JGR Solid Earth

RESEARCH ARTICLE
10.1029/2024JB028857

Key Points:
- We obtained the fine crust-mantle structure of tectonic boundaries in NE China using Rayleigh wave phase velocities and receiver functions
- The tectonic boundaries Chifeng-Kaiyuan Fault and Tan-Lu Fault are both whole-crustal faults with strong seismic activity
- The upper mantle of North China Craton exhibits low S-wave velocity with strong seismic activity

Supporting Information:

Supporting Information may be found in the online version of this article.

Correspondence to:

T. Xu and Y. Ai,
xutao@mail.iggcas.ac.cn;
ysai@mail.iggcas.ac.cn

Citation:

Yang, T., Xu, T., Ai, Y., Yang, J., & Yuan, H. (2024). Fine crust-mantle structure of the major tectonic boundaries between the North China Craton and Central Asian Orogenic Belt revealed from Rayleigh wave phase velocities and receiver functions. *Journal of Geophysical Research: Solid Earth*, *129*, e2024JB028857. https://doi.org/10.1029/2024JB028857

Received 31 JAN 2024
Accepted 1 JUL 2024

Author Contributions:

Conceptualization: Tingwei Yang, Tao Xu, Huaiyu Yuan
Data curation: Tao Xu, Yinshuang Ai
Formal analysis: Huaiyu Yuan
Funding acquisition: Tao Xu, Yinshuang Ai
Investigation: Tingwei Yang, Jinhui Yang
Methodology: Tingwei Yang
Resources: Tao Xu, Yinshuang Ai
Software: Tingwei Yang
Supervision: Tao Xu, Huaiyu Yuan
Writing – original draft: Tingwei Yang
Writing – review & editing: Tingwei Yang, Tao Xu, Yinshuang Ai, Jinhui Yang, Huaiyu Yuan

Fine Crust-Mantle Structure of the Major Tectonic Boundaries Between the North China Craton and Central Asian Orogenic Belt Revealed From Rayleigh Wave Phase Velocities and Receiver Functions

Tingwei Yang[1,2,3], Tao Xu[1,3], Yinshuang Ai[3,4], Jinhui Yang[3,5], and Huaiyu Yuan[6,7]

[1]Key Laboratory of Mineral Resources, Institute of Geology and Geophysics, Chinese Academy of Sciences, Beijing, China, [2]University of Chinese Academy of Sciences, Beijing, China, [3]Innovation Academy for Earth Science, Chinese Academy of Sciences, Beijing, China, [4]Key Laboratory of Earth and Planetary Physics, Institute of Geology and Geophysics, Chinese Academy of Sciences, Beijing, China, [5]State Key Laboratory of Lithospheric Evolution, Institute of Geology and Geophysics, Chinese Academy of Sciences, Beijing, China, [6]ARC Center of Excellence from Core to Fluid Systems, Macquarie University, Sydney, NSW, Australia, [7]Centre for Exploration Targeting, School of Earth Sciences, The University of Western Australia, Perth, WA, Australia

Abstract The Tanlu Fault Zone (TLFZ) and Chifeng-Kaiyuan Fault (CKF) serve as tectonic boundaries between the North China Craton (NCC) and the Central Asian Orogenic Belt (CAOB). Clarifying the refined structure of these tectonic boundaries is crucial for understanding the relationships between the tectonic units and the heterogeneity in the destruction of the NCC. In this study, two linear seismic arrays were deployed across these tectonic boundaries. Based on the phase velocity dispersion and receiver functions extracted from the seismic arrays, the Hamiltonian Monte Carlo algorithm was employed for the joint inversion of the S-wave velocity (Vs) in the crust and uppermost mantle. The Vs model was then used to correct the time differences in common conversion point (CCP) stacking. The CCP stacking results indicate that the boundary faults TLFZ and CKF are both whole-crustal faults that separate the NCC and CAOB. The Vs structure showed a significant low-velocity anomaly in the mantle beneath the NCC, with intense seismic activity within the crust. This suggests that the NCC was affected by the subduction of the Western Pacific, leading to crustal and mantle destruction. In contrast, the CAOB exhibited a clear high-velocity anomaly with relatively stable crustal structures. We believe that the NCC and CAOB have undergone structural modification and destruction due to the closure of the Paleo-Asian Ocean and the activities of the TLFZ since the Late Mesozoic. During the Cenozoic, the region east of the TLFZ experienced more significant destruction in the NCC than the other adjacent tectonic units.

Plain Language Summary The joint inversion of Rayleigh wave phase velocities and receiver functions provides a reliable method for obtaining high-precision S-wave velocity (Vs) models. Here, we applied a joint inversion based on the Hamiltonian Monte Carlo algorithm to acquire detailed crust-mantle Vs models in Northeast China and utilized this velocity structure to constrain the common conversion point (CCP) stacking to obtain a more reliable Moho depth. A comprehensive high-resolution seismological model was established by integrating the Vs model, Moho depth, Vp/Vs ratio, and seismic activity. We then revealed the differential structural features and seismic heterogeneity on both sides of the tectonic boundaries between the Central Asian Orogenic Belt (CAOB) and the North China Craton (NCC). Our research results offer new constraints on the crust and upper mantle structure in Northeast China, contributing to the understanding of the geodynamic context underlying the differential structures between the CAOB and the NCC and the characteristics of their boundaries.

1. Introduction

Northeast China is comprised of two major tectonic units: the North China Craton (NCC) and the Central Asian Orogenic Belt (CAOB). The NCC is one of the oldest cratons in the world (Santosh et al., 2009; Tang et al., 2016), whereas the CAOB, located north of the NCC, is considered as the world's largest ancient accretionary orogenic belt (Kröner et al., 2014; Wilde, 2015). In northeast China, there are two first-order regional structural features: the Chifeng-Kaiyuan Fault and the Tan-Lu fault zone (CKF and TLFZ in Figure 1). The CKF is commonly considered the tectonic boundary between the NCC and the CAOB (Liu et al., 2017; Xiao et al., 2003; Zhang,

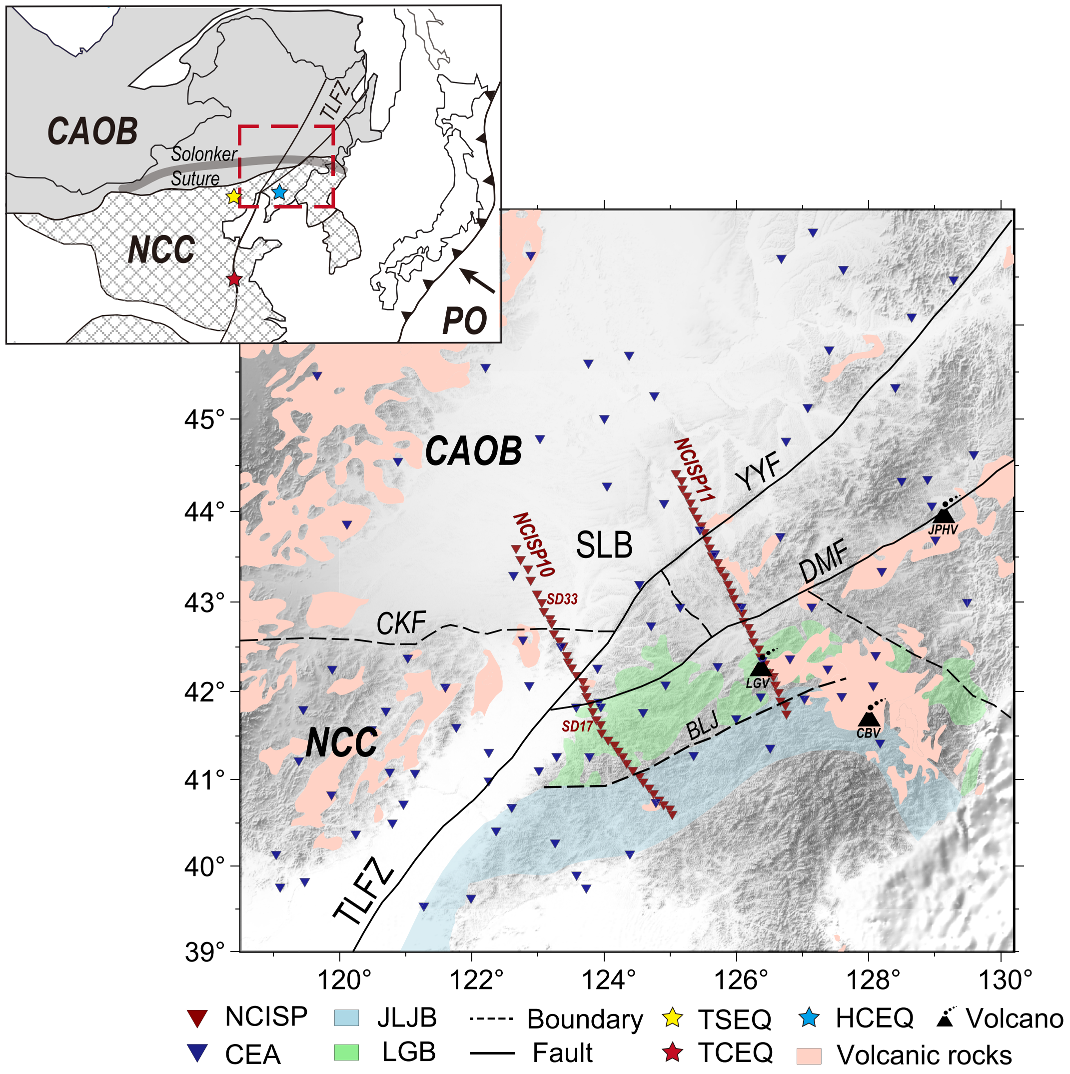

Figure 1. Tectonic units and major faults in NE China. NCC, North China Craton; CAOB, Central Asian Orogenic Belt; TLFZ, Tan-Lu Fault Zone; SLB, Songliao basin; YYF, Yilan-Yitong fault; CKF, Chifeng-Kaiyuan fault; DMF, Dunhua-Mishan fault; LGB, Longgang Block; JLJB, Jiaoliaoji Belt; BLJ, boundary of Longgang Block and Jiaoliaoji Belt; LGV, Longgang Volcano; JPHV, Jingpohu Volcano; CBV, Changbai Volcano; Red triangles NCISP from Institute of Geology and Geophysics, Chinese Academy of Sciences; Blue triangles CEA from China Earthquake Administration; For the small image in the upper left corner, PO, Pacific Ocean; Black arrow signifies the direction of tectonic plate subduction; Gray indicates the region of CAOB; White grid indicates the region of NCC; Gray strip indicates Solonker suture zone; Yellow star TSEQ, Tangshan earthquake; Red star TCEQ, Tancheng earthquake; Blue star HCEQ, Haicheng earthquake.

Zhao, et al., 2014). It probably formed during the Early Paleozoic but was reactivated during the closure of the Paleo-Asian Ocean along the Solonker suture zone in the Late Permian-Early Triassic (Figure 1), resulting in the amalgamation of the NCC and the CAOB into a unified landmass (Figure 1). The TLFZ was formed during the Late Mesozoic era due to the northwestward subduction of the Paleo-Pacific Plate beneath East Asia. This subduction resulted in the southward subduction of the Mongol-Okhotsk oceanic lithosphere (Schettino & Scotese, 2005; Xiao et al., 2015), causing left-lateral strike-slip movements along the TLFZ, which subsequently deformed a significant region in East Asia (Huang et al., 2015). During this period, the left-lateral strike-slip motion in the northern TLFZ cut across the CKF (the original boundary between the NCC and CAOB), leading to a segmentation of the Dunhua-Mishan Fault (DMF) between the two offsetting CKF portions, forming the boundary between the NCC and CAOB (Gu et al., 2018; Xu et al., 2000).

Despite extensive research on the geometric, kinematic, and dynamic characteristics of the CKF, the exact location of the spatial contact of this boundary between the NCC and CAOB remains heavily debated (Liu et al., 2019; Q. Yang et al., 2024) because of limited rock exposure and extensive Cenozoic sediment coverage. Additionally, a clear understanding of its deep extension, fault properties, and role in the NCC destruction process is still lacking. Distinct structures in the present-day lithosphere (Wilde, 2015; Zhang, Gao, et al., 2014) have been reported across these fault zones, suggesting that regional-scale boundaries may have played critical roles in the amalgamation, reworking, or destruction of the NCC. However, crust and shallow lithospheric upper mantle models are generally lacking in this area due to the paucity of seismic deployments. This requires a detailed investigation of the deep structures to understand the complex nature of NCC destruction along the fault zone.

In contrast to the distinct lithospheric structure across the CKF, the TLFZ is a major zone of significant magmatic and seismic activity in the eastern Eurasian continent (Wu et al., 2005, 2011; Xu et al., 2013). The northern segment of the TLFZ serves as a boundary, and most volcanic activity in Northeast China occurs in the eastern region (Zhang et al., 2018). However, current evidence regarding magma structures near the tectonic boundary is insufficient, making it challenging to elucidate the causes and distribution of magmatic activity. Consequently, a better understanding of the present-day thermal state differences in the lithosphere on either side of the tectonic boundary remains elusive. Additionally, the seismic activity on either side of the TLFZ is unevenly distributed, with the main fault being relatively seismically inactive and frequent earthquakes occurring on the eastern side (Chen et al., 2020). Specifically, a devastating M_S7.8 magnitude earthquake struck Tangshan on 28 July 1976, in the northeastern part of the NCC (Zhu et al., 2012). Another significant event was the Haicheng M_S7.3 earthquake, which occurred in the northern segment of the TLFZ in 1975, further indicating that the TLFZ is still active today (Zheng et al., 2018). Therefore, understanding the differences in crust-mantle structures across the TLFZ and uneven seismic activity is important to explain the relationship between magmatic and seismic activities resulting from the destruction of the NCC.

To address these issues, we deployed two linear arrays, NCISP10 and NCISP11, consisting of 72 three-component Guralp-CMG-3T seismometers with an observation frequency bandwidth of 120 s to 50 Hz. NCISP10 spanned the TLFZ and CKF, whereas NCISP11 extended across the TLFZ and Longgang volcanic areas (Figure 1). Utilizing the seismic data from these profiles, we employed an inversion method based on the HMC algorithm to jointly invert receiver functions and surface waves. Additionally, we combined H-κ stacking and Common Conversion Point (CCP) stacking (Zhu & Kanamori, 2000) to obtain the crust-mantle S-wave velocity (Vs) model, Moho depth, and crustal Vp/Vs ratio at the intersection of the northern segment of the TLFZ and CKF. Our aim was to acquire information on the extension and internal structural characteristics of the tectonic boundary between the NCC and the CAOB under the complex background of strike-slip movement along the northern segment of the TLFZ and to provide additional geophysical evidence for the uneven shallow responses in the eastern and western parts of the TLFZ, likely resulting from the destruction of the NCC.

2. Tectonic Setting and Previous Studies

Northeast China is situated on the northeastern margin of the Eurasian continent and encompasses the overlapping zones of the Pacific and Paleo-Asian tectonic domains. Our study area encompassed the northeastern section of the NCC and the southeastern margin of the CAOB. The NCC formed 1.85 billion years ago through the amalgamation of two Archean continental blocks, and underwent sedimentation until the Mesozoic, after which it was intensively reworked or destroyed (Zheng et al., 2017). The CAOB is positioned between the NCC and Siberian Craton and is recognized as the world's largest accretionary orogenic belt, with significant crustal growth and transformation during the Phanerozoic (Xiao et al., 2003). The Solonker suture zone, located north of the NCC, is widely accepted as the ultimate suture zone in the Paleo-Asian Ocean.

During the Paleozoic, the Paleo-Asian Oceanic Plate subducted beneath the NCC, shaping an Andes-type continental margin along its northern boundary (Windley et al., 2007; Xiao et al., 2003, 2015). In the Early to Middle Triassic, a collision occurred between the southern margin of Siberia (South Mongolia) and the NCC, which resulted in large-scale thrusting to the south. This led to the overthrusting of subduction-accretionary complex rocks within the CAOB onto the NCC (Zhang, Gao, et al., 2014). During the Jurassic to Cretaceous period, the eastern NCC experienced severe destruction due to the subduction of the Paleo-Pacific plate (Wang & Li, 2008; Zhu et al., 2011, 2012). Previous studies have demonstrated that destruction of the NCC predominantly occurred east of the Taihang Mountains, leading to substantial thinning of the cratonic lithosphere. The thickness of the lithosphere decreased from approximately 200 km during the Paleozoic era to less than 100 km today (Figure S1 in Supporting Information S1) (Meng et al., 2021; Zhu et al., 2011, 2012).

The northern TLFZ, a larger strike-slip fault east of the Taihang Mountains, traverses the entire NCC and CAOB from south to north. Near the northern NCC, the TLFZ bifurcates into two branches, the DMF and Yilan-Yitong faults (YYF), which crosscut and displace the CKF (Figure 1). Previous studies have suggested that complex mantle convection may exist beneath the TLFZ, causing significant historic seismicity such as the 1668 M_S8.5 Tancheng earthquake (Lei et al., 2020). The TLFZ and its adjacent regions exhibit extensive crustal and subcrustal magma intrusions with a widespread distribution of alkaline basalts (Li et al., 2018; Menzies et al., 2007). Specifically, the area east of the TLFZ corresponds to an alkaline basaltic eruption since the Neogene, such as those in the Changbai Mountains, Jingpo Lake, and Longgang areas (Figure 1). In contrast, there have been few reports on volcanic rocks in the Songliao Basin west of the TLFZ since 28 million years ago.

In recent years, numerous geophysical studies have been conducted in Northeast China, providing valuable insights. These include the recognition of the nappe structure of the CAOB on the NCC (Zhang, Gao, et al., 2014) and the development of a large mantle wedge model formed by the westward subduction of the Pacific Plate (Lei & Zhao, 2005). For details, see Lei et al. (2023). The lithosphere on the eastern side of the TLFZ was slightly thinner (~80 km) than that on the western side (~100 km) (Meng et al., 2021). There were also distinct variations in the velocity structures on both sides (Guo, Chen, et al., 2016; Guo et al., 2018). These studies have revealed the primary characteristics of the crust-mantle structure in Northeast China, providing abundant deep structural information for investigating the lithospheric structural features, tectonic evolution, and dynamic causes on both sides of the tectonic boundary. However, current achievements have mostly focused on the macroscopic features of the tectonic boundary in Northeast China. Detailed delineation of the complex structures and fracture patterns within tectonic boundaries remains challenging, making it difficult to understand the reasons behind the evident deep and shallow structural differences in the lithosphere across tectonic boundaries. Simultaneously, the relationship between the northern segment of the TLFZ, a significant zone of magmatic and seismic activity in northeast China, and the destruction of the NCC is yet to be clarified.

3. Data and Methods

3.1. Seismic Data

The broadband seismic stations used in this study were the NNW-SSE trending NCISP10 and NCISP11 profiles (Figure 1). These profiles extended from within the Songliao Basin to the YYF and DMF. Profile NCISP10 consists of 38 seismic stations covering a span of approximately 370 km. It extends from northeast to southwest, successively crossing the CKF, YYF, and DMF. The array was operated between October 2016 and July 2018. Profile NCISP11, parallel to NCISP10, comprises 34 seismic stations spanning approximately 330 km. It crosses the YYF and DMF successively and the Longgang volcano. The array recorded continuous waveforms between July 2018 and December 2019. Both profiles have an average station spacing of 10 km.

3.2. Receiver Functions

Receiver functions (Langston, 1977, 1979; Phinney, 1964; Vinnik, 1977) contain extensive information on converted waves and multiple reflections generated by velocity discontinuity interfaces beneath seismic stations. They are widely used to invert the detailed crustal and upper-mantle velocity structures (Zheng et al., 2005). We chose teleseismic events with epicentral distances within the range of 30°–90° and moment magnitudes greater than 5.5 (Figure S2 in Supporting Information S1). The event records were bandpass-filtered from 0.01 to 5 Hz, and we computed the radial receiver functions for teleseismic seismic P-waves through time-domain iterative deconvolution (Ligorría & Ammon, 1999). We used a Gaussian filter coefficient of 5.0 to filter the receiver functions.

In this study, we have followed the quality control methods proposed by Shen et al. (2013): (a) We first exclude the RFs with amplitudes exceeding a threshold (Discarding those with amplitude values less than zero at time 0 s). (b) The receiver functions were convolved with the vertical components of the seismic records to generate synthetic seismograms. Subsequently, we compared these synthetic seismograms with actual data. Receiver functions with a poor fit (variance reduction <0.8) were removed (Figure S3 in Supporting Information S1). (c) The receiver functions from the same station were stacked into average receiver functions for each back-

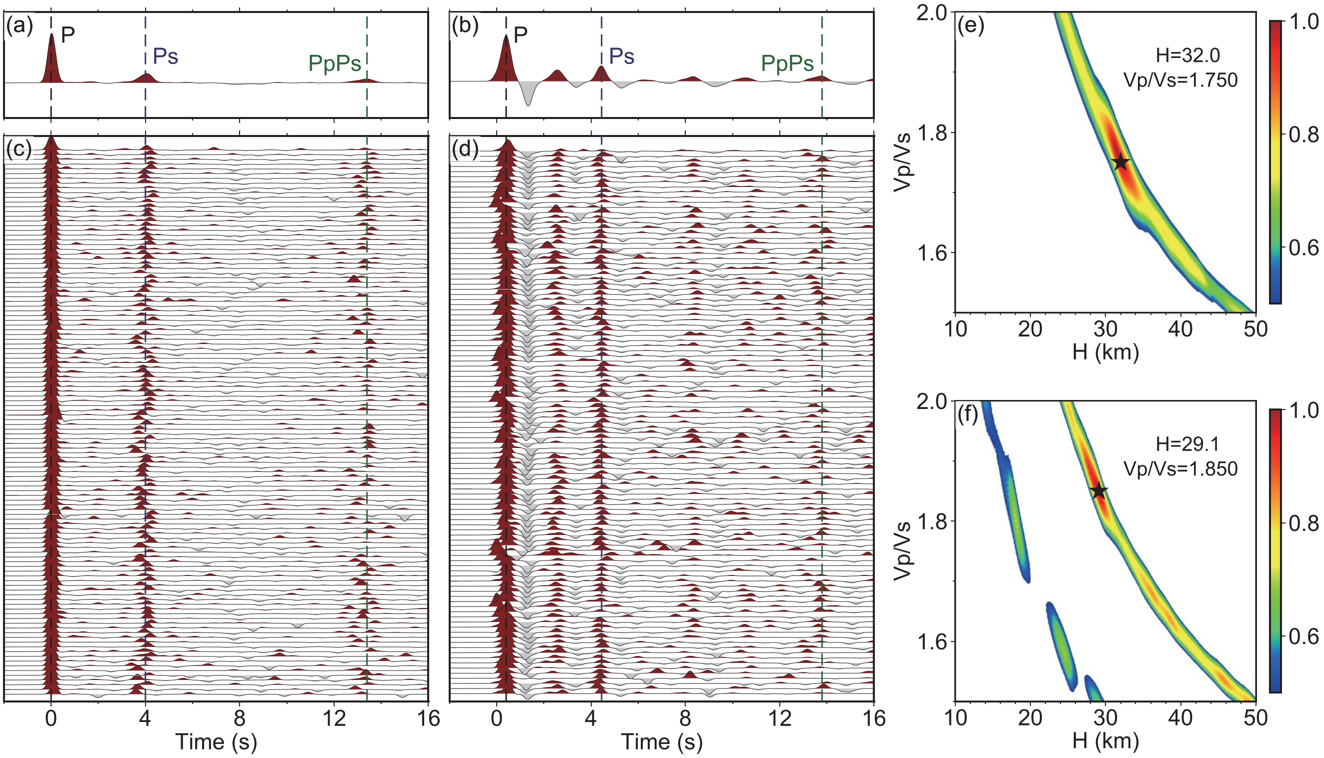

Figure 2. The stacking receiver function of SD17 and SD33 (a) and (b); All of the effective receiver functions (c) and (d); The results of H-κ stacking at SD17 and SD33 (e) and (f).

azimuthal sector (divided into 30° bins), and we removed receiver functions with significant differences from the corresponding sector-averaged receiver functions (cross-correlation coefficient <0.5) (Li et al., 2020) (Figure S4 in Supporting Information S1). Finally, we kept 5,988 high-quality receiver functions with clear conversion and multiple waves.

As an example, we show the RFs for station SD17 located within the NCC and station SD33 located within the Songliao Basin (Figure 2). Within the NCC, the RFs usually have a high signal-to-noise ratio and a clear Ps phase from the Moho surface, which is consistent with the ancient and stable nature of cratons that usually possess simple crustal structures (Tang et al., 2016). In contrast, the RFs observed at station SD33, situated in the Songliao Basin, were noticeably affected by the sedimentary layers, displaying multiple phases originating from the shallow sedimentary interface. We demonstrated the delay phenomenon of the receiving function P-waves in the basin using synthetic data testing (Figure S5 in Supporting Information S1). We primarily focused on employing the resonance removal filter proposed by Yu et al. (2015) (Figure S6 in Supporting Information S1), along with joint inversion methods, in order to mitigate the impact of sedimentary layers on the receiver functions (Figure S7 in Supporting Information S1). The Ps phase of the Moho surface is still clear despite being affected by the sedimentary layers (Figures 2b and 2d). We then calculated stacked receiver functions for each station (Figures 3a and 4a).

3.3. Rayleigh Wave Phase Velocities

We associated the portable stations along the NCISP10 and NCISP11 profiles with 98 permanent stations in the China Earthquake Administration network (Figure 1). We implemented a data processing workflow based on the methodology proposed by Bensen et al. (2007) to calculate cross-correlation functions from the ambient noise data (Figure S8 in Supporting Information S1). Specifically, the daily vertical component waveform data from all stations were instrument response-removed, bandpass-filtered between 3 and 80 s, and subjected to time-domain normalization and spectral whitening to mitigate the impacts of large earthquakes and balance the frequency spectrum of ambient noise (Y. Yang et al., 2007). Subsequently, we calculated the cross-correlation functions for all overlapping station pairs and linearly stacked them to enhance the surface wave signals. We then performed a

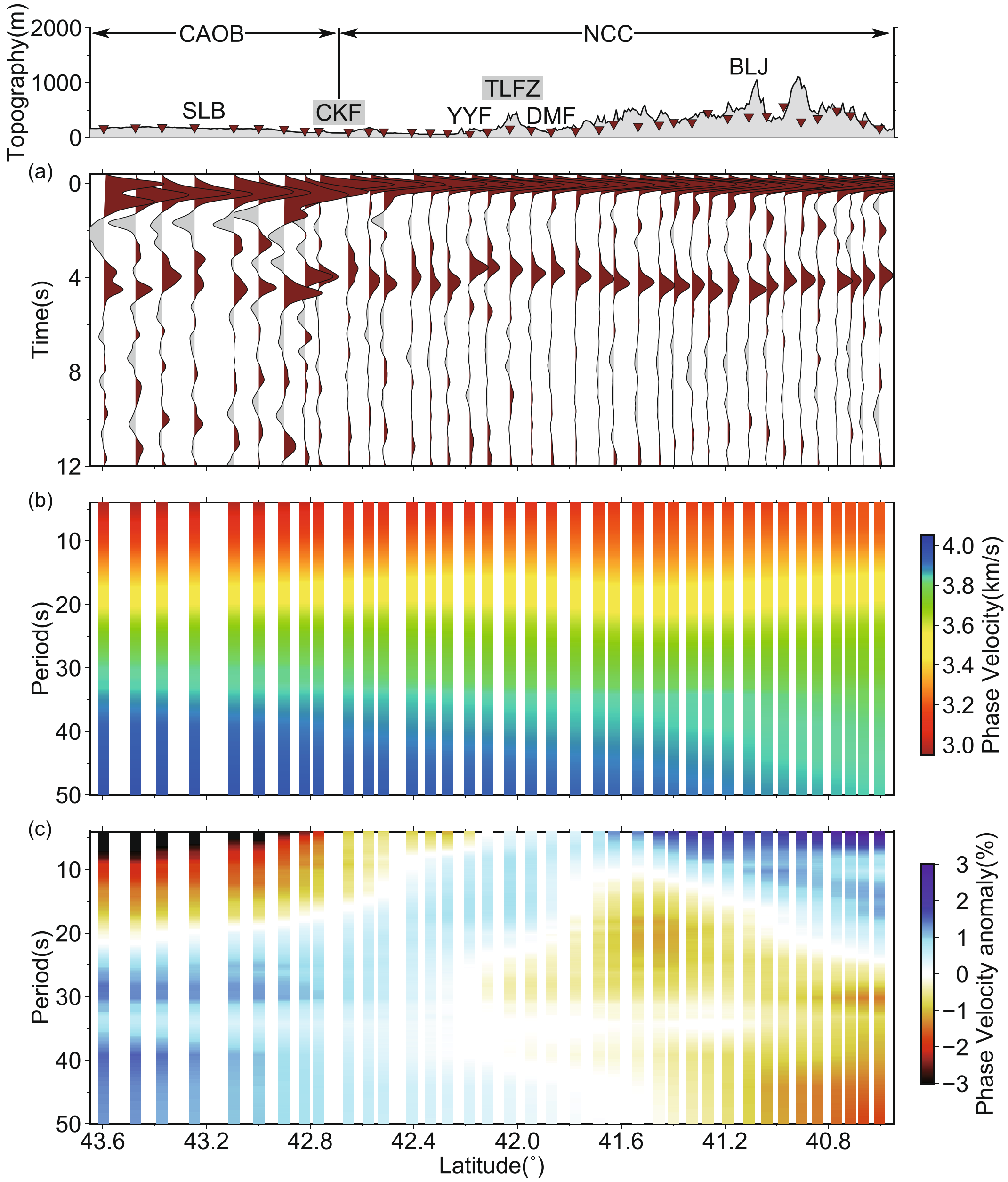

Figure 3. Stacking receiver functions and phase velocities at the NCISP10 profile. (a) Stacking receiver functions; (b) Phase velocity dispersion curves; (c) Phase velocity anomaly.

time-frequency analysis using narrowband and phase-matching filters through the automated frequency–time analysis (AFTAN) technique (Levshin & Ritzwoller, 2001) in order to measure the phase velocity dispersion curves.

The quality of these dispersion data serves as the foundation for the subsequent inversion. For quality control of the dispersion curves, the following criteria were applied. (a) It is generally required that the station spacing exceed three times the wavelength to satisfy the far-field assumption (Bensen et al., 2007). However, recent studies have shown that effective dispersion curves can be obtained with station spacings longer than 1.5 times the wavelength or even equal to the wavelength (Guo, Yang, & Chen, 2016; Luo et al., 2015). To balance the data quantity and signal-to-noise ratio (SNR), in this study we used cross-correlation data with station spacings longer than 2 times the wavelength (The SNR defined the same as that in Bensen et al. (2007)). (b) Quantitative selection of the effective dispersion data was based on the SNR, and we ultimately used cross-correlation data with an SNR

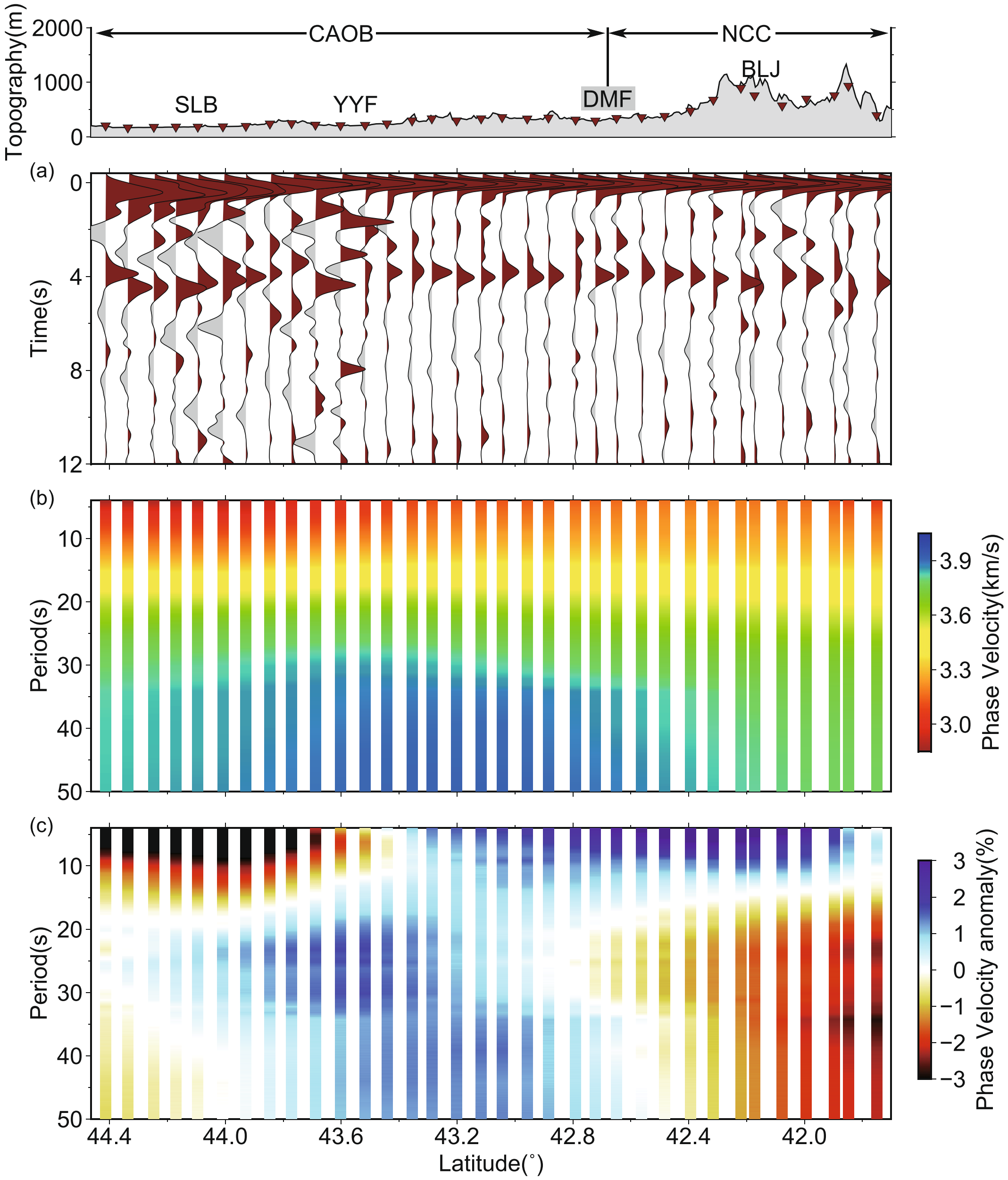

Figure 4. Stacking receiver functions and phase velocities at the NCISP11 profile. (a) Stacking receiver functions; (b) Phase velocity dispersion curves; (c) Phase velocity anomaly.

exceeding 10 (Yao et al., 2010). (c) As the phase velocity of adjacent station pairs reflects a comprehensive response to close subsurface media, the dispersion curves between adjacent station pairs should also be similar (Nakata et al., 2019) (Figure S9 in Supporting Information S1). When the dispersion curves for a particular station pair showed a significant disparity, they were excluded. It should be noted that we only kept dispersion curves within 3 times the standard deviation of these adjacent station pair data. (d) The smoothness of the dispersion curve is challenging to quantify but is an important reference for selecting effective data. The phase velocity for each period reflects the overall response of subsurface structures within a certain depth range, resulting in smooth dispersion curves (Knopoff et al., 1966). We computed the synthetic dispersion curves generated from the average crustal velocity model, which were then compared with the raw dispersion data. Excessively rough or smooth dispersion data were eliminated by comparing them with synthetic dispersion curves generated using the regional average model. Specifically, gradient values of the dispersion data that were three times larger than those of the synthetic curves were considered very rough, whereas a gradient equal to zero was deemed smooth, and the corresponding data were removed.

Following quality control processing, we acquired 9,908 phase velocity dispersion curves within a period range of 4–35 s (Figure S10 in Supporting Information S1). Assuming that surface waves propagate along great-circle paths, we utilized the regionalized imaging method developed by Montagner and Nataf (1986) to invert the pure path dispersion curves (Yao et al., 2010) (Figure S11 in Supporting Information S1). Figures 3 and 4 show the stacked receiver functions with an equivalent pulse width for a Gaussian coefficient of five and the Rayleigh wave phase velocity dispersion curves along the NCISP10 and NCISP11 profiles. The spatial continuity of the Pms phase in the receiver functions was traceable along both profiles, and the corresponding travel times exhibited clear regional variations. From the Songliao Basin (SLB) to the YYF, the Pms arrival times were found to be approximately 4 s, whereas under the Boundary of the Longgang Block and Jiaoliaoji Belt (BLJ), they were delayed to approximately 4.5 s. The overall undulation of the in-phase axis is consistent with the topography. To expand the period range of the phase velocity dispersion curves, we utilized earthquake surface wave dispersion data (a range–35–50 s) released by Fan et al. (2021) (Figure S12 in Supporting Information S1). The phase velocity periods in this study covered a range of 4–50 s, indicating a sensitivity to deeper structures. The overall phase velocities along both profiles exhibit a good linear increasing trend and demonstrate regular variations (Figures 3b and 4b). In the period range of 4–10 s, the Songliao Basin, with thicker sedimentary layers, displayed distinct low-phase velocities (Figures 3c and 4c). During the period range of 30–50 s, the phase velocity beneath the NCC was found to be lower than that beneath the CAOB (Figures 3c and 4c).

3.4. HMC Joint Inversion of Rayleigh Wave Phase Velocities and Receiver Function

The receiver function method has become important for studying discontinuities (velocity gradients) within the Earth's interior (Phinney, 1964). In comparison, Rayleigh wave dispersion curves have been shown to be more sensitive to absolute Vs (Shapiro et al., 2005). Therefore, the joint inversion of these two data sets can simultaneously provide more accurate information about interfaces and volumetric velocity variations (Julià et al., 2000; Suwen et al., 2023; Xu et al., 2022). The HMC is a hybrid Monte Carlo method based on the Hamiltonian system in theoretical mechanics (MacKay, 2003). This algorithm makes full use of the derivatives of the probability distribution with respect to the model parameters to accelerate the search in the model space. It can efficiently sample the probability density in the shortest possible time, reduce dependency on samples, and avoid issues related to low acceptance rates. In this study, we consider using the HMC for the joint inversion of Rayleigh wave phase velocities and the receiver function for inverting the fine crust-mantle Vs model.

Specifically, the concept of HMC treats model parameters as particles in phase space. These particles move from their current positions (current model) to new positions (proposed model) along the trajectory. The trajectory of the particles is a function of time and governed by Hamilton's equation (Fichtner et al., 2019; Landau & Lifshitz, 2013),

$$\frac{\mathrm{d}m_i}{\mathrm{d}t} = \frac{\partial H}{\partial p_i}, \frac{\mathrm{d}p_i}{\mathrm{d}t} = -\frac{\partial H}{\partial m_i} \tag{1}$$

where m_i is the generalized position of the particle along its trajectory, p_i is the generalized momentum of the particle at the current moment, and t is a time variable. The Hamiltonian $H(\mathbf{m}, \mathbf{p})$ is the total energy of the particle, expressed as the sum of the potential and kinetic energy.

$$H(\mathbf{m}, \mathbf{p}) = U(\mathbf{m}) + K(\mathbf{p}) \tag{2}$$

where $U(\mathbf{m})$ is potential energy, and $K(\mathbf{p})$ is kinetic energy.

The HMC is used to sample from an auxiliary distribution in a 2n-dimensional (n dimensions each for position and momentum) space by marginalizing the components of the momentum space to obtain posterior samples. We define the potential energy function as the likelihood function of the posterior distribution of the model parameters **m** according to the observed data **d**. The $U(\mathbf{m})$ and $K(\mathbf{p})$ are defined as follows.

$$K(\mathbf{p}) = \frac{1}{2}\sum_{i,j=1}^{n} p_i M_{ij}^{-1} p_j \tag{3}$$

$$U(\mathbf{m}) = -\log \rho_{\mathrm{m}}(\mathbf{m}|\mathbf{d}) \tag{4}$$

where M is mass matrix, and ρ_m is conditional probability density function.

We assume that the Hamiltonian equations define the energy function for the joint state of the generalized positions **m**, and generalized momenta **p**. Their joint probability distribution is given by

$$\rho_{\mathrm{c}}(\mathbf{m},\mathbf{p}) = \exp[-H(\mathbf{m},\mathbf{p})] = \rho_{\mathrm{m}}(\mathbf{m}|\mathbf{d})\exp\left(-\frac{1}{2}\sum_{i,j=1}^{n} p_i M_{ij}^{-1} p_j\right) \tag{5}$$

We employ the Leapfrog algorithm to solve the Hamiltonian equations, which can ensure energy conservation. The current state of the particle $(\mathbf{m}, \mathbf{p})$ propagates along the Hamiltonian trajectory for a certain time τ, updating the particle's position and momentum, resulting in a new state $(\mathbf{m}_\tau, \mathbf{p}_\tau)$. The acceptance rate of the proposed state is calculated using the Metropolis algorithm.

$$min\left[1, \frac{\rho_{\mathrm{c}}(\mathbf{m}_\tau, \mathbf{p}_\tau)}{\rho_{\mathrm{c}}(\mathbf{m},\mathbf{p})}\right] = min\left[1, \mathrm{e}^{-H(\mathbf{p}_\tau)+H(\mathbf{p})}\right] \tag{6}$$

If it is accepted, the new state $(\mathbf{m}_\tau, \mathbf{p}_\tau)$ is retained. Otherwise, it remains in the current state $(\mathbf{m}, \mathbf{p})$. Theoretically, the acceptance ratio is 1, as indicated by the conservation of Hamiltonians.

In this study, we used the HMC global optimization algorithm to conduct a joint inversion of the Rayleigh wave phase velocities and receiver functions. The potential energy function $U(\mathbf{m})$ is defined as the joint misfit of the receiver functions and surface wave dispersion curves as follows,

$$U(\mathbf{m}) = \frac{W_1}{2}\sum_{j=1}^{m}\left(G_j^{Rf}(\mathbf{m}) - Rf_j^{obs}\right)^2 + \frac{W_2}{2}\sum_{k=1}^{n}\left(G_k^{Swd}(\mathbf{m}) - Swd_k^{obs}\right)^2 \tag{7}$$

where $G_j^{Rf}(\mathbf{m})$ and $G_k^{Swd}(\mathbf{m})$ represent the forward operators of the receiver functions and Rayleigh wave phase velocities, respectively. The variable **m** represent the model parameters (Vs and thickness), and Rf_j^{obs} and Swd_k^{obs} represent the observed data for the receiver functions and surface wave dispersion curves, respectively. The weight matrix $\boldsymbol{W}_1$ and $\boldsymbol{W}_2$ are designed based on Julià et al. (2000).

$$\begin{aligned} \boldsymbol{W}_1 &= \mathrm{diag}\left\{\sqrt{\frac{w}{N_{Rf}\left(\sigma_l^{Rf}\right)^2}}, l = 1,2,\ldots N_{Rf}\right\} \\ \boldsymbol{W}_2 &= \mathrm{diag}\left\{\sqrt{\frac{1-w}{N_{Swd}\left(\sigma_l^{Swd}\right)^2}}, l = 1,2,\ldots N_{Swd}\right\} \end{aligned} \tag{8}$$

where w is a parameter ranging from 0 to 1, which is adjusted based on the inversion results (Du et al., 2021). N is the number of data and σ is standard variations of data sets.

To validate the feasibility and stability of the inversion method, we conducted tests on synthetic data (Figure 5). Receiver functions are sensitive to velocity discontinuities, whereas phase velocities are sensitive to the Vs values, which is beneficial for obtaining a more accurate Vs model. Aleardi et al. (2020) emphasized that the dimensionality can be determined by standard statistical tools such as chi-square (χ^2) or Bayesian information

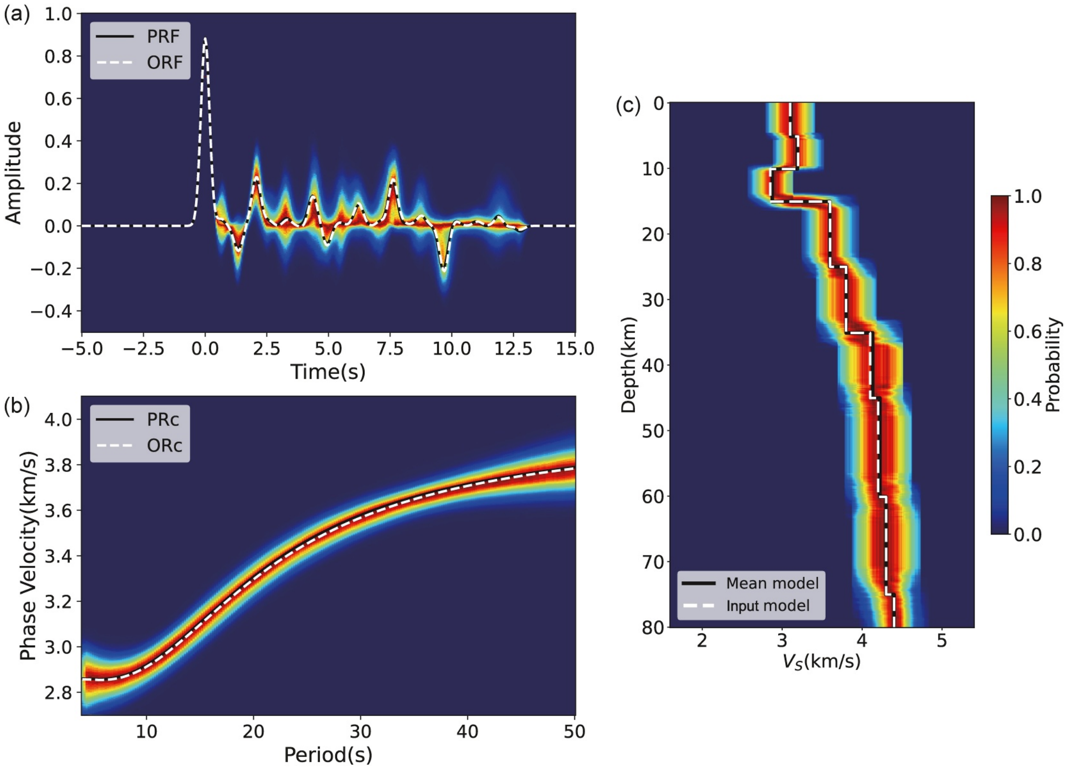

Figure 5. Joint inversion result of the synthetic data with HMC framework. (a) Receiver function fitting; (b) phase velocity dispersion curve fitting. (c) Inversion result of Vs model. The dotted white lines in (a) and (b) show the synthetic data and the dotted white line in (c) presents the synthetic data from input model. The black lines in (a) and (b) represent the predicted data, while the black line in (c) illustrates the mean of the posterior distribution at each depth.

criterion (BIC) (Sambridge et al., 2006; Schwartz, 1978). The most probable number of layers was selected based on these common statistical tools (Table S2 in Supporting Information S1). Additionally, given that the phase velocity is more sensitive to variations in Vs than to Vp and density (Dahlen & Tromp, 1999), it is customary to invert solely for variations in Vs while deriving Vp and density using Brocher's relations (Brocher, 2005). The 9-layer model is justified as it offers a balanced trade-off between model complexity and goodness-of-fit, demonstrated by a moderate BIC and a relatively low χ^2, suggesting that it captures the data information effectively while avoiding overfitting (Table S2 and Figure S13 in Supporting Information S1). Hence, we establish a 9-layer one-dimensional model for inversion, with the thickness and Vs values as the inversion parameters, by employing the Hamiltonian Monte Carlo (HMC) algorithm for the simultaneous inversion, as described above. Finally, we obtained the average model parameters from a group of models with the minimum misfit. The fitting of the data was satisfactory (Figures 5a and 5b), the recovered model matched the input model (Figure 5c), and the statistical plots of the posterior models followed a theoretical distribution (Figure 6). This indicates that the HMC global optimization method for the joint inversion of receiver functions and surface wave dispersion curves can correctly obtain the Vs model beneath the stations.

4. Results

4.1. S-Wave Velocity

We have applied the joint inversion method to the actual data recorded by 72 broadband seismic stations along the NCISP 10 and NCISP 11 profiles. The HMC algorithm is less affected by the initial model (Figure S14 in Supporting Information S1). Our initial model was based on a three-dimensional Vs model for the Northeast China region obtained through surface wave dispersion data inversion from Shen et al. (2016). In the model parameterization, we determined the thickness of the low-velocity sedimentary layer by synthetic tests, establishing an approximate average thickness of 0.3 km (Figure S5 in Supporting Information S1). The depth of the

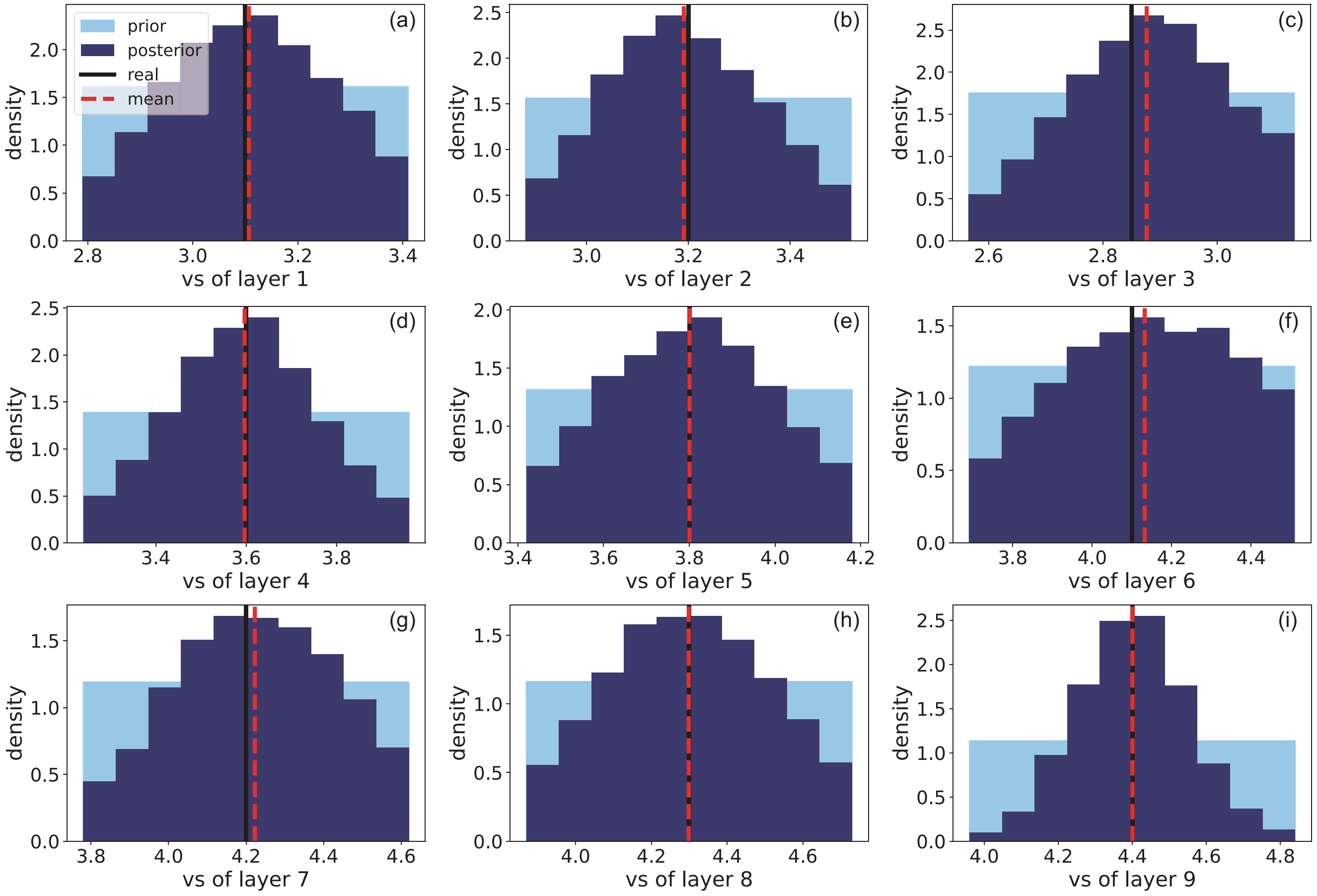

Figure 6. Posterior distribution of the model parameter. The true parameters are shown in the solid black line, and mean values are shown in dotted red line.

Moho was determined by averaging the one-dimensional model proposed by Shen et al. (2016). By computing the velocity gradient relative to the depth, we derived an average initial Moho depth of 32 km. As an example, we show the fitting of receiver functions and dispersion curves as well as the obtained Vs results for stations SD17 and SD33 (Figures 7 and 8). The SD17 station, located in the NCC (Figure 1), exhibited clear Ps phases in the receiver functions, with arrival times of approximately 4 s (Figure 7a). The phase–velocity dispersion curve was relatively smooth (Figure 7b). The high signal-to-noise ratio and clean data led to a relatively simple final inversion result for Vs (Figure 7c), which is consistent with prior knowledge of ancient and stable cratonic crust. On the other hand, the receiver functions of the SD33 station, located in the Songliao Basin (Figure 1), are influenced by low-velocity sedimentary layer, resulting in a delayed direct P-wave phase, and the appearance of multiple phases associated with sedimentary interface around 2.5 s (Figure 8a). The Ps phase from the Moho surface at SD33 also exhibited a noticeable delay, around 4.5 s (Figure 8a). Moreover, there was a significant decrease in the phase velocity in the 4–10 s range below SD33 station (Figure 8b), indicating the presence of a low-velocity layer in the shallow subsurface, which was reflected in the Vs model (Figure 8c). Overall, the fitting of the data from the two stations, including the receiver functions and dispersion curves, demonstrated satisfactory performance, and the obtained Vs results aligned well with the surface geology.

Utilizing HMC joint inversion, we obtained one-dimensional Vs models beneath 72 stations along the NCISP 10 and NCISP 11 profiles. The overall Vs model beneath the profiles was displayed through interpolation based on the interstation spacing and layer thickness. The results illustrate the detailed versus models beneath profiles NCISP 10 and NCISP 11 (Figures 9c and 10c). On a larger scale, there was a noticeable correlation between the shallow Vs and topography (Figures 9c and 10c). The areas southeast of both profiles, where the elevation is higher, exhibited a relatively higher velocity. In contrast, the areas to the northwest of both profiles, with lower

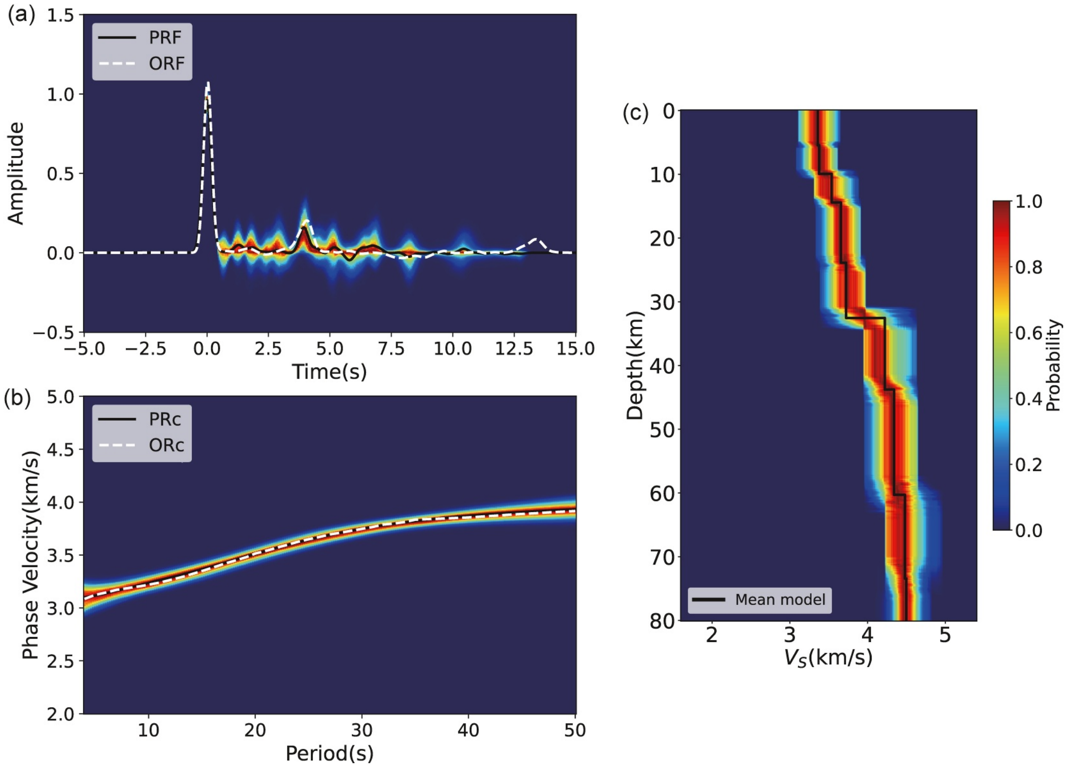

Figure 7. Joint inversion result of SD17 with the HMC framework. (a) Receiver function fitting; (b) phase velocity dispersion curve fitting. (c) Inversion result of the Vs model. The dotted white lines in (a) and (b) show the real data. The black lines in (a) and (b) represent the predicted data, while the black line in (c) illustrates the mean of the posterior distribution at each depth.

elevations and thicker sedimentary cover in the Songliao Basin, had lower velocities. Overall, this pattern reflects the characteristics of mountainous uplift in the higher regions and basin depressions in the lower regions.

At shallow depths beneath the Songliao Basin, Vs was notably influenced by sedimentary deposits. The distribution of the lower velocity in this region strongly aligns with the geological boundary of the Songliao Basin marked by the CKF (Figures 9c and 10c). Across the CKF, the northwest side, characterized by shallow sedimentary low-velocity layers within the Songliao Basin, exhibits a significant discontinuity with the NCC. The Vs results for the middle crust about 15 km beneath the Songliao Basin show a high-velocity anomaly of approximately 4.00 km/s (III in Figures 9c and 10c), in contrast to the 3.6 km/s Vs in the crust on the southeast side of the boundary in the NCC. Both sides exhibit distinct characteristics in the upper mantle. There is a clear high-velocity body of 4.7 km/s at depths of 40–60 km in the upper mantle beneath the SLB situated on the northwest side of the boundary (II in Figures 9c and 10c). Two low-velocity anomalies of less than 4.2 km/s were observed within a depth range of 40–60 km in the upper mantle beneath the TLFZ and at the boundary of the Longgang Block and Jiaoliaoji Belt, both on the southeast side of the boundary (I-a and I-b in Figures 9c and 10c).

In addition, we calculated the average Vs for each layer and computed the percentage of anomalies relative to the average, providing a more intuitive representation of the velocity anomalies (Figure 11). The results of the relative velocities of both profiles clearly show significant differences in the upper mantle Vs between the NCC and CAOB (Figure 11). In the southern NCC, Vs was generally lower than that in the northern CAOB (Figure 11). Significant low-velocity anomalies were observed near the TLFZ and Longgang Volcano (I in Figures 9c and 10c), which is consistent with the results of Fan et al. (2021) (Figure 11). There were also clear high-velocity features near the lower crust and also the upper mantle in the Songliao Basin, which is in agreement with the findings of Tang et al. (2022) (Figure 11). This consistency confirmed the reliability of the inversion results.

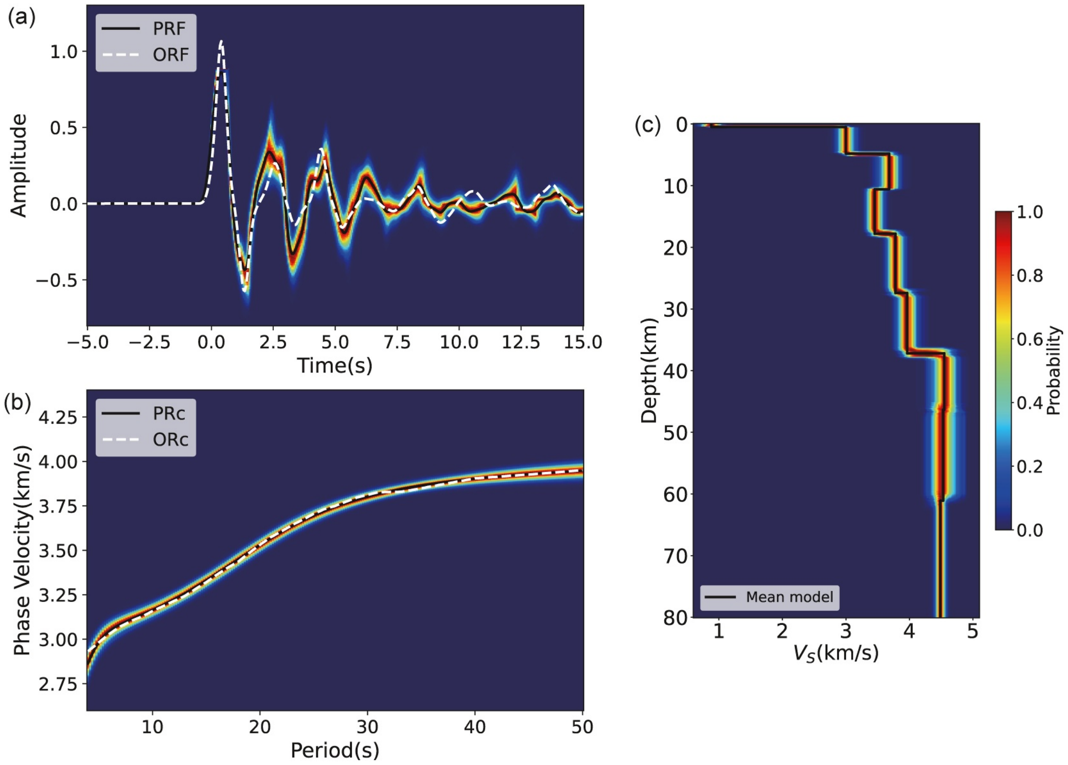

Figure 8. Joint inversion result of SD33 with the HMC framework. (a) Receiver function fitting; (b) phase velocity dispersion curve fitting. (c) Inversion result of the s model. The dotted white lines in (a) and (b) show the real data. The black lines in (a) and (b) represent the predicted data, while the black line in (c) illustrates the mean of the posterior distribution at each depth.

4.2. Moho Depth

The receiver function H-κ stacking method is mainly used in order to obtain the average the crustal thickness and Vp/Vs ratio below the arrays (Figures 9 and 10). In the case of a linear observation system composed of multiple stations, the P-wave Receiver Function Common Conversion Point (CCP) stacking technique can be used to study velocity discontinuity information within Earth's interior (Zhu & Kanamori, 2000). Typically, a later arrival of the Moho phase in the receiver function indicates a deeper Moho. However, the results for the Moho depth are also affected by the velocity model in the process of time-depth conversion, especially the influence of low-velocity layers beneath the basins. To obtain more accurate Moho depths, a more precise crustal velocity structure was required as input for CCP stacking (Figures S16 and S17 in Supporting Information S1). Therefore, we used the Vs model from the joint inversion to constrain the time-depth conversion in CCP stacking processing. The width of the stacking bin was set as 6 km along the profile direction. We conducted robustness tests for CCP stacking using various stacking bin schemes, as detailed in Figures S18 and S19 in Supporting Information S1. We obtained relatively accurate undulations in the Moho beneath profiles NCISP 10 and NCISP 11 (Figures 9e and 10e). The results show that the Moho depth varies between 32 and 38 km in both profiles and exhibits some non-uniformity along the profiles (Figures 9e and 10e). Specifically, the Moho depth showed a negative correlation with topography, with deeper Moho depths of approximately 38 km in the higher-elevation area of the Jiaoliaoji Belt, which has rugged terrain. The shallow part is approximately 32 km deep in the Songliao Basin and is low and flat. This is consistent with a Moho depth of approximately 32 km in the western Songliao Basin obtained by Zhang et al. (2020) using receiver function migration imaging. To validate the accuracy of the Moho depth, we used the Receiver Function H-κ stacking method to obtain Moho depth points beneath the stations. The results of these two methods were consistent (green dots in Figures 9e and 10e). Xu et al. (2017) conducted a deep seismic reflection profile with a length of approximately 600 km spanning the northern part of the TLFZ, revealing Moho depths between 25 and 39 km. The Moho depths from our profiles agree very well with the deep reflection data in the northern part of our study area, thus confirming the reliability of our imaging results.

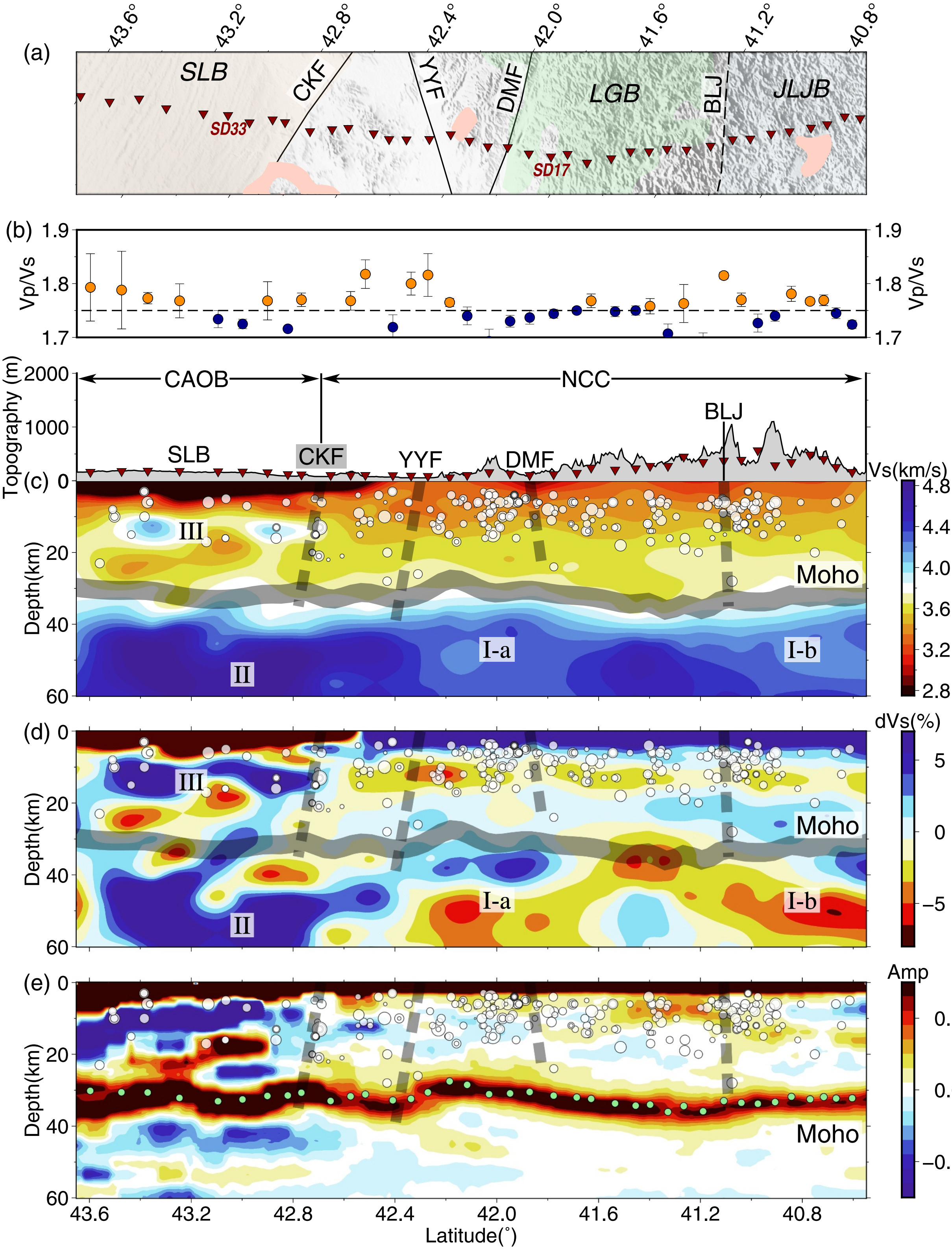

Figure 9. Interpreted seismic images across NCISP 10. (a) Geological map near the NCISP10 profile; (b) Vp/Vs ratio calculated by H-κ stacking; (c) Vs obtained from joint inversion; (d) Vs anomaly maps; (e) CCP stacking image. The thick gray dashed line represents the fault, and the gray solid line represents the Moho. The green dots represent the Moho depth calculated by H-κ stacking; The white dots denote the earthquakes with magnitudes greater than 3.0 that occurred between 1970 and 2022, and these earthquakes were within 50 km from the migrated profile.

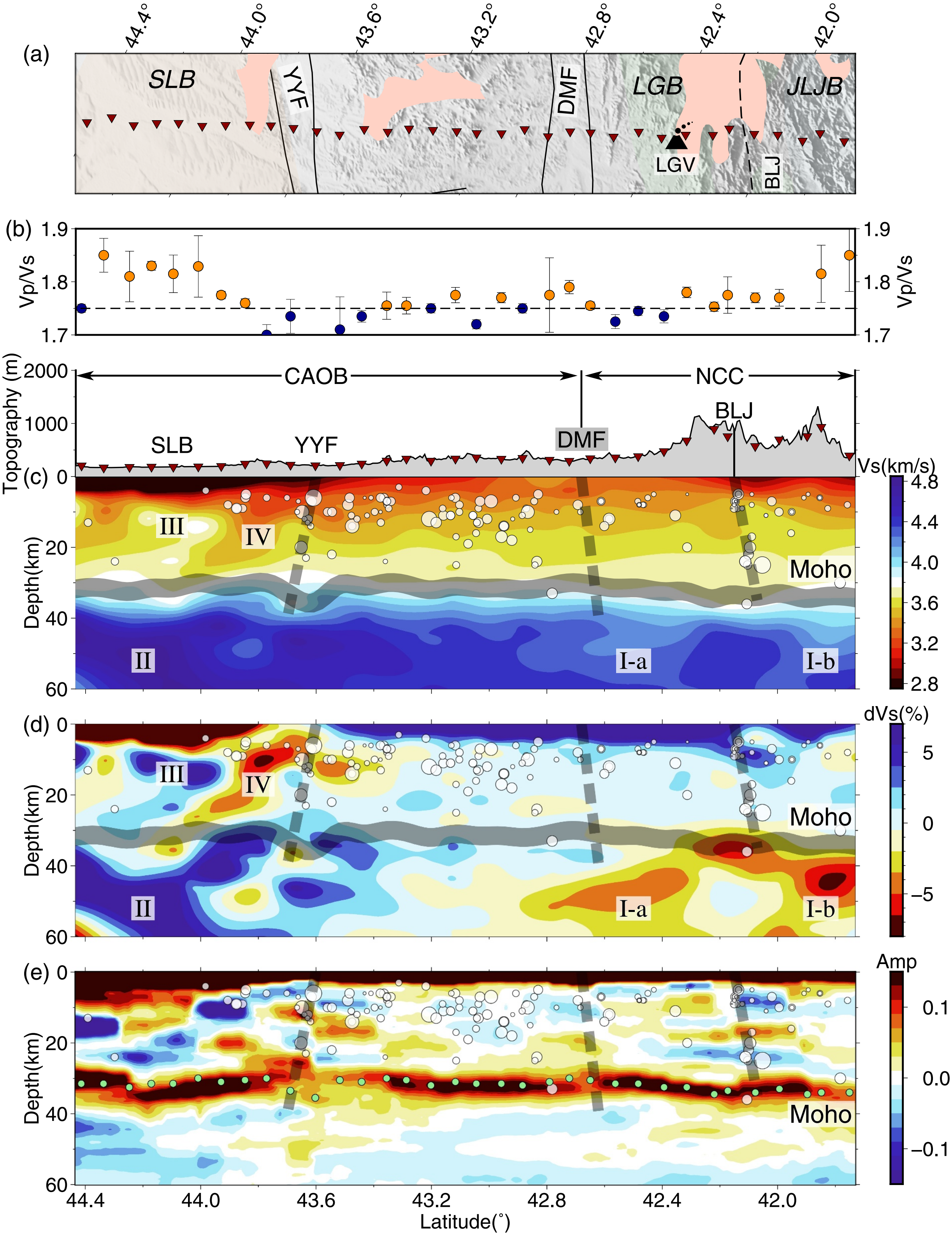

Figure 10. Interpreted seismic images across NCISP 11. (a) Geological map near the NCISP11 profile; (b) Vp/Vs ratio calculated by H-κ stacking; (c) Vs obtained from joint inversion; (d) Vs anomaly maps; (e) CCP stacking image. The thick gray dashed line represents the fault, and the gray solid line represents the Moho. The green dots represent the Moho depth calculated by H-κ stacking; The white dots denote the earthquakes with magnitudes greater than 3.0 that occurred between 1970 and 2022, and these earthquakes were within 50 km from the migrated profile.

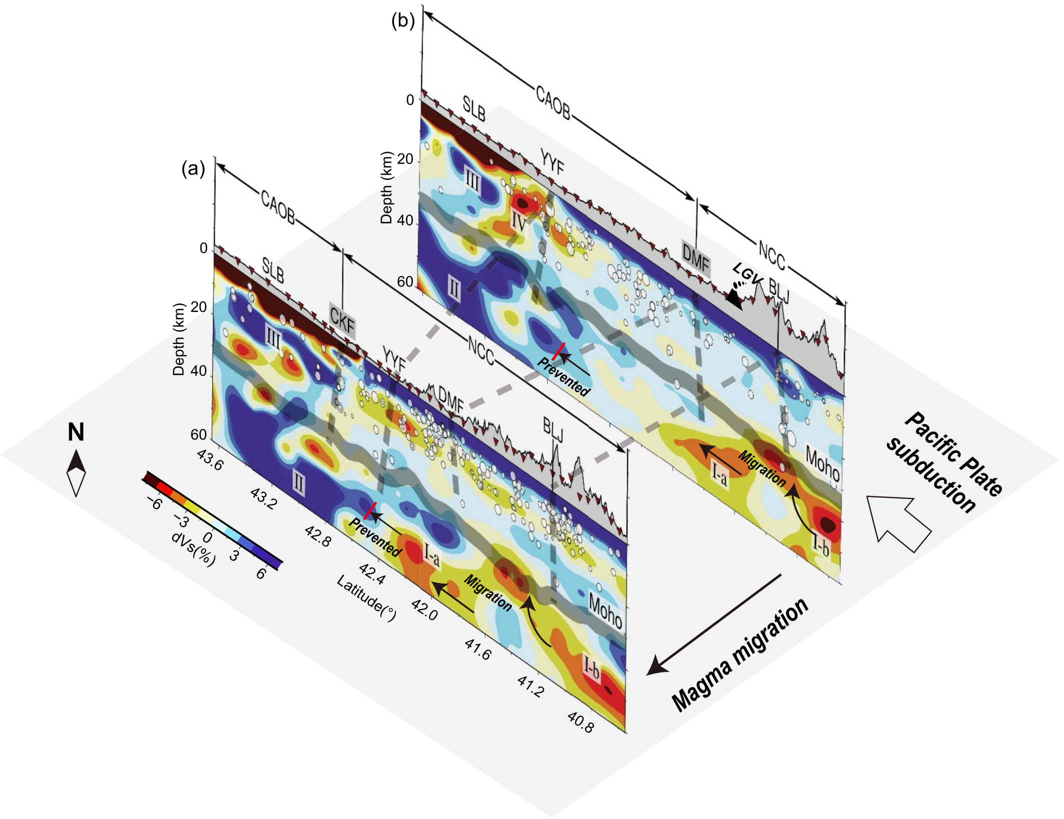

Figure 11. Vs anomaly maps at NCISP10 (a) and NCISP11 (b). The thick gray dashed line represents the fault, and the gray solid line represents the Moho. The white arrow indicates the direction of Pacific Plate subduction; The black arrows indicate the magma distribution; The white dots denote the earthquakes with magnitudes greater than 3.0 that occurred between 1970 and 2022, and these earthquakes were within 50 km from the migrated profile.

In general, similar Moho structures reflect consistent blocks or domains, each with a unique evolutionary history. Pronounced Moho depth changes are usually found near tectonic boundaries such as the TLFZ, CKF, and BLJ. Interestingly, only YYF was found to exhibit a Moho discontinuity in NCISP 10 (Figure 9e). However, both profiles displayed a Moho discontinuity beneath the YYF and the DMF in NCISP 11 (Figure 10e). Based on the distribution of seismic activity and geological investigations, we preliminarily characterized the characteristic morphology and extension depth of the YYF and DMF (dashed lines in Figures 9e and 10e, marked as YYF and DMF).

The Moho depth variation beneath the CKF and the northwestern-dipping trend of the Moho depth on both sides of the fault together provide a reference for characterizing the deep features of the CKF (Figure 9e). We integrated CCP stacking, Vs anomalies, and seismic activity results to outline the burial depth and trend characteristics of the CKF. Figures 9e and 10e show a significant difference in the Moho depth between the Longgang Block and the Jiaoliaoji Block. The Moho beneath the Longgang Block is deeper, whereas that in the Jiaoliaoji Block is shallower, with distinct block boundaries (BLJ). Figure 10e shows the existence of several multiple-phase reflections (alternating positive and negative multiple phases) in the crust at depths of 5–25 km beneath the Longgang Block. These multiple phases and the Moho Ps phase were both discontinuous at the BLJ (Figures S20 and S21 in Supporting Information S1). This crustal phase pattern is consistent with the characteristics of the Moho Ps phase, with a large number of earthquakes (magnitudes greater than 3). Combining the CCP stacking results with previous shallow geological data (Peng et al., 2016), we outlined the preliminary burial morphology of the BLJ region and suggested that the BLJ crustal fault marks the boundary between the Jiaoliaoji Orogen and the Longgang Block (dashed lines in Figures 9e and 10e, marked as BLJ).

5. Discussion

5.1. Major Tectonic Boundary in Northeast China

It is widely accepted that the Solon suture zone between the NCC and CAOB marks the closure of the Paleo-Asian Ocean (Windley et al., 2007; Xiao et al., 2003; Zhang, Gao, et al., 2014). Because of the Neogene sedimentary cover, it is challenging to precisely determine the structural boundary between the NCC and CAOB on the surface, resulting in ongoing debates regarding its exact location. As shown in Figure 9c, there was a clear discontinuity in Vs on both sides of the CKF, and the velocity structures exhibited significant differences. The seismic distribution also forms a linear alignment, particularly near coordinates 42.7°N and at depths of 0–15 km. Our results indicate the non-uniformity of the geological structures on both sides of the CKF and significant seismic activity in the vicinity of the fault. We propose that the high-velocity anomaly (III in Figures 9d and 10d) beneath the CAOB west of the CKF represents an ancient crystalline basement of the CAOB that did not appear in the crust beneath the NCC east of the fault.

From a macroscopic perspective, beneath the NCISP 10 profile, the region west of the CKF, which corresponds to the CAOB, experienced less seismic activity. In contrast, the region to the southeast, representing the NCC, exhibited greater seismic activity due to tectonic features such as the YYF, DMF, and BLJ (Figures 9 and 10). The CCP stacking results suggest that the Moho Ps phase beneath the Songliao Basin differs significantly from that beneath the NCC (Figures 9e and 10e), which corresponds to the relatively low Vs anomaly (Figures 9d and 10d) in the Songliao Basin. These results also reflect the structural differences and activity on both sides of the CKF. Therefore, our results support the idea that the CKF represents a major geological boundary between the NCC and the CAOB in Northeast China (Xiao et al., 2003; Zhang, Gao, et al., 2014).

Orogenic events in the northeastern accretionary zone of the NCC occurred between the Permian and Triassic periods (Wang et al., 2015; Wilde, 2015). In the Early Cretaceous, the TLFZ extended into Northeast China. Significant sinistral displacement in the DMF occurred during the Late Mesozoic, leading to a segment of the DMF between the displaced CKF constituting the boundary of the NCC and CAOB (Figure 10e). As shown in Figure 10d, the NCC exhibits a large low-Vs anomaly in the upper mantle south of the boundary, whereas the CAOB features a prominent high-velocity anomaly. This demonstrates significant nonuniformity on both sides of the velocity structural boundary. Beneath the NCISP 11 profile, the YYF is a boundary, with seismic activity in the NCC to the south being stronger than that in the CAOB to the north (Figure 10). The results for the NCISP 10 profile demonstrate similar findings, except for the CKF as the boundary. Overall, the upper mantle beneath the northwestern region of the study area, corresponding to the CAOB, exhibited a high-velocity anomaly with reduced seismic activity. By contrast, the southeastern region, representing the NCC, features a significant low-velocity anomaly in the upper mantle with increased seismic activity. This reflects the differences in the geological structure and seismic activity between the NCC and CAOB at the mantle scale.

In terms of regional tectonic components, the NCC in the study area can be further divided into two subdomains, the JiaoLiaoJi Orogenic Belt and the Longgang Block, separated by another structural boundary, denoted as the BLJ (Figure 1). JiaoLiaoJi is one of the three Paleoproterozoic orogenic belts that developed within the NCC and it extends northeastward. The formation of the JiaoLiaoJi Orogenic Belt remains a subject of debate, with two prevailing evolutionary models: the rift orogenic model and the arc-continent collision model (Dong et al., 2022; Luo et al., 2008; Zhao et al., 2012). The arc-continent collision model proposes that the southern margin of the Longgang Block was once a passive continental margin. Subsequently, the Paleo-oceanic plate to the south was subducted southward, giving rise to an intraoceanic arc. Eventually, this arc collided with the Longgang Block during the late Paleoproterozoic era (Faure et al., 2004; Lu et al., 2006). The CCP stacking results of this study revealed multiple instances of Ps phase axis discontinuity within the crust at depths of 0–25 km beneath the boundary defined by the BLJ between the Longgang Block and the JiaoLiaoJi Orogenic Belt (Figure 10e, Figures S20 and S21 in Supporting Information S1). Moreover, a significant Ps phase discontinuity appeared in the seismic phase transitions near a depth of 37 km (Figure 10e, Figures S20 and S21 in Supporting Information S1). All of these discontinuities are indicative of thrust faults and they support previous geological interpretations of the southward subduction polarity of the Longgang Block. Peng et al. (2016), using the analysis of gravity and electromagnetic data and the study of rock physical properties in the region, suggested that during the early stages of the BLJ formation, a boundary fault controlled by a basin developed, constituting the original structural boundary. There are differences in the metamorphic processes between the LGB and JLJB (Cai et al., 2020). These are considered to be the boundary between the LGB and JLJB, and there is a thrust structure in the structural analysis (Li et al., 2005). Hence, by combining the earthquake distribution and also the surface location, we can infer that the BLJ is a slightly rising thrust fault on the right side (Figure S21 in Supporting Information S1). This conclusion aligns with our geological inference that the BLJ represents the boundary between the secondary structural units (Figures 9 and 10).

5.2. Crust-Mantle Characteristics Beneath the TLFZ

The northern segment of the TLFZ bifurcates into the YYF and DMF and spans the NCC and CAOB. The TLFZ exhibited intricate deep-seated structural characteristics, making it challenging to discern its fine structure. We utilized geological data analyses from fieldwork conducted in the DMF area by Huang et al. (2015) and detailed field survey results from the YYF area by Gu et al. (2016) to determine the fault surface location. We identified a westward-dipping low-Vs zone west of the YYF, located at approximately 43.5°N, at depths of 0–15 km (IV in Figures 10c and 10d). This low-Vs zone extended downward to approximately 20 km. Such tilted low-Vs zones or areas with strong lateral velocity gradients are often interpreted as regions where faults are located (Thurber et al., 1997; Wang et al., 2008). By combining previous research on the shallow positions of the faults, along with our results on velocity anomalies, Ps phase discontinuity, and seismic activity distribution, we delineated the fault orientations of the YYF and DMF (Deng et al., 2013; Gu et al., 2017; Tang et al., 2010). We further propose that the YYF trends to the northwest, whereas the DMF trends northeast. Our results also indicate that the YYF cuts through the Moho, representing a large-scale strike-slip fault in Northeast China (Figures 9 and 10), which is consistent with previous conclusions that the northern segment of the TLFZ is a crustal or even lithospheric-scale fault system (Deng et al., 2013; Gu et al., 2017). Figure 9e demonstrates that the YYF exhibits a 2–3 km down-dip offset of the hanging wall relative to the footwall, indicating a normal faulting feature. The stretching direction of the YYF was nearly perpendicular to the subduction direction of the Pacific Plate. Our results support the idea that the rift stage of the northern segment of the TLFZ may represent a far-field, shallow response to the rollback of the Northwestern Pacific slab subduction on the eastern edge of the Asian continent (Uyeda & Kanamori, 1979).

Owing to the lack of detailed kinematic analyses of the northern segment of the TLFZ, many questions regarding the extensional or strike-slip movements that occurred within the YYF and DMF remain unresolved. The extensive magmatic activity beneath the northeastern region of China suggests that extensional tectonics along the YYF developed during the Early Cretaceous (Zhang et al., 2011). The subduction of the Pacific Plate led to a series of compressional and tectonic inversion structures located in northeastern China (Ge et al., 2010). Xu et al. (2017) utilized active-source deep reflection seismic profiles to reveal that the YYF underwent an initial negative flower structure (a negative flower structure generated on top of strike-slip faults experiencing transform extension) that transitioned to a positive flower structure in later stages. The CCP stacking below the YYF in the NCISP10 profile exhibited characteristics of normal faulting, reflecting the extensional state of the lower crust and upper mantle (Figure 9e). In the northern part of the NCISP11 profile beneath the YYF, there is a slight upward shift in the hanging wall, and the Moho is unclear at the location of the YYF, possibly because the fault structure is less well defined, with the Moho on both sides of the fault occurring at nearly the same depth. This suggests that the fault in this area may have compressional or strike-slip characteristics (Figure 10e). Based on previous research, we propose that the current morphology of the YYF may be the result of multiple stages of tectonic inversion involving both compression and extension, leading to a complex geological structure (Gu et al., 2017; Tang et al., 2010). We can speculate that the intersection of the YYF and DMF primarily has an extensional nature (Figure 9), whereas it exhibits a compressional or strike-slip nature as it extends northward (Figure 10). Figure 9e does not show any significant Moho depth change in the Moho beneath the DMF along the NCISP10 profile, suggesting that the DMF is not the major rupture point at the intersection. However, in the northern part of the NCISP11 profile, there was a clear Ps phase discontinuity near DMF. This suggests that the DMF, extending northward from the intersection, cuts through the crust and behaves as a strike-slip fault roughly parallel to the YYF (Figure 10e).

5.3. Magmatic Activity Beneath the LGV

Since the Late Cretaceous, Northeast China has experienced significant tectonic-magmatic events triggered by the subduction of the Pacific Plate (Wu et al., 2003), as suggested by the “Big Mantle Wedge” model proposed by Lei and Zhao (2005). According to this model, the Pacific Plate subducts westward by introducing water-bearing material into the deep mantle. Subsequent dehydration of these materials occurs within the mantle transition zone, leading to the addition of fluids in the upper mantle, which causes melting and upwelling of the upper mantle, resulting in magmatism, including that seen in the Changbai Mountains. Figure 11 demonstrates that, with the TLFZ as the boundary, the velocity characteristics of the lithospheric mantle exhibit an overall pattern of "low in the east, high in the west." Some researchers have suggested that the Weifang segment of the TLFZ potentially serves as a conduit for the sustained upward movement of hot and wet materials from the mantle to the Earth's surface upon intrusion into the crust (Ma et al., 2020, 2022; Tian et al., 2020). Figure 10c reveals a distinct upper mantle low Vs (<4.3 km/s) beneath Longgang Volcano at depths of 30–50 km. This low Vs anomaly is also noted in the model published by Fan et al. (2021). It is suggested that Vs below 4.3 km/s in the mantle can not be achieved based solely on temperature and composition effects (Wang et al., 2009), and that Vs lower than 4.25 km/s can be indicative of partial melting in the upper mantle, especially in areas beneath volcanic activity (Plank & Forsyth, 2016). Fan and Chen (2019) used ambient noise imaging to identify low-Vs anomalies beneath the Longgang Volcano and Jingbo Lake Volcano, located southeast of the TLFZ. They proposed that the alkaline basalt eruptions from the Changbai volcanic group since the Neogene have led to the accumulation of hot melt in the lithospheric mantle, forming magma reservoirs and providing heat and material sources for volcanoes. Song and Lei (2023), using the inversion of phase velocity dispersion curves, identified a widely distributed mid-lower crustal low-velocity layer beneath the entirety of NE China. They suggested that this layer connects with upper crust features beneath the volcanoes, implying potential exchanges among these volcanic regions (Song & Lei, 2023). Combined with the above tectonic set, the observed low Vs (<4.3 km/s) beneath Longgang Volcano is likely related to volcanic activity, which is also associated with clustered seismic sources beneath the BLJ.

Geochemical sample analysis near the northern segment of the TLFZ also revealed the presence of calc-alkaline basalts north of the YYF and DMF. Ling et al. (2017) utilized new geochemical and geochronological data on volcanic rocks and related rocks in the YYF and DMF regions and suggested that these faults underwent extensional strike-slip motion during 124–100 Ma period. This aligns with our inference that the low-velocity upper mantle region beneath the Longgang Volcano is associated with magmatic activity. They further speculated that this was due to the subduction of the Paleo–Pacific Plate, which resulted in the northward migration of volcanic activity along the fault zone. Fan et al. (1999) analyzed the geochemical composition of the Longgang Volcano rocks and suggested that the volcano originated from mantle-derived magma ascent processes with minimal evolution and crustal contamination. It did not undergo a crustal magma chamber stage and formed only a single-type basaltic rock zone. This corroborates our inference of magmatic activity beneath the Longgang Volcano based on the low-velocity upper mantle region. Moreover, Vp/Vs ratios can serve as another crucial parameter for characterizing crustal structure and composition (Christensen, 1996; Yuan, 2015). When the magma cools, the differences in magma composition are often effectively reflected in the average Vp/Vs ratio (Yuan, 2015). For instance, an average Vp/Vs ratio less than 1.75 is commonly interpreted as indicating felsic composition, while higher Vp/Vs ratios are frequently associated with mafic/ultramafic components (Christensen, 1996). According to receiver functions H-κ stacking, it was found that the Longgang Volcano exhibits higher Vp/Vs ratios (>1.75) beneath the BLJ. Corresponding to the lower Vs in the upper mantle and the higher Vp/Vs in the crust in the horizontal location (Figures 9b and 10b), we have speculated that the influence of magma upwelling related to the Pacific Plate subduction could be responsible for the region beneath the Longgang Volcano (Fan & Chen, 2019; Shan et al., 2021; Song & Lei, 2023), and the BLJ with clustered seismic sources likely provided a channel for magma upwelling (Peng et al., 2016).

Another interesting feature was the widespread high Vs anomaly observed beneath the Songliao Basin (Figure 11). This finding is consistent with those of previous studies. Guo et al. (2015) obtained Vs values for the crust and upper mantle in the northeastern region using a joint inversion of the surface wave and receiver functions. They identified an extensive high-velocity anomaly beneath the Songliao Basin and proposed the existence of a thick and coherent mantle lid beneath it, revealing small-scale mantle convection in the Changbai Mountain volcanic area, Songliao Basin, and Greater Khingan Range. The Songliao Basin acts as a downflow counterpart to the upwelling flow in the Changbai Mountain volcanic area. Meng et al. (2021) proposed that the dense lithospheric mantle beneath the Songliao Basin acts as a barrier, impeding the penetration of hot material from the asthenosphere. Tang et al. (2022) obtained inversion results showing fast Vs at depths of approximately 40–100 km and suggested that the dense mantle lid beneath the Songliao Basin might hinder the migration of asthenospheric melt to the surface. Xu et al. (2023) detected anisotropy beneath the Songliao Basin, displaying a circular distribution in the fast direction. They linked this observation to a persistent high-velocity anomaly in the upper mantle, indicating early lithospheric subsidence. In our model, we also found a prominent high-Vs layer at depths of 40–80 km beneath the Songliao Basin, which corresponded to the dense mantle lid. Combining previous viewpoints with the extensive outcrops of volcanic rocks in the study area (pink in Figure 1; Hao et al., 2016), we suggest that this upper mantle lid not only prevents the migration of asthenospheric melt to the surface but also blocks the eastward migration of abundant magmatic activity beneath the Longgang Volcano. Typically, when magmatic upwelling is obstructed, it tends to intrude into weak lithospheric zones. Therefore, we hypothesize that the asthenospheric melt in the study area eventually migrated and was channeled to the geological boundaries of the Songliao Basin, represented by CKF, YYF, and DMF, resulting in localized upwelling flows reaching the surface (Figure 11). In summary, we believe that the east-to-west variation in the lithospheric mantle velocity on both sides of the TLFZ is a primary indicator of eastward-high and westward-low lithospheric temperatures (Figure 11). The dense mantle lid beneath the Songliao Basin obstructed the eastward migration of magmatic activity, making the TLFZ a significant boundary for thermal state differences in the Cenozoic lithosphere.

6. Conclusion

We conducted joint inversions of the surface wave dispersion curves and receiver functions using the HMC algorithm, which provided Vs beneath the NCISP10 and NCISP11 profiles. Based on this Vs model, we constrained CCP stacking to obtain detailed Moho undulations beneath the NCISP10 and NCISP11 profiles. Based on the seismic activity analysis, we draw the following conclusions:

1. Regarding the tectonic boundary between the NCC and the CAOB in northeastern China, we considered the CKF as the boundary in the Liaoning segment, whereas the TLTZ (DMF) as the boundary in the Jilin segment. This verifies the structural evolution of the Paleo-Asian Ocean closing along the CKF and later being subjected to strike-slip faulting of the YYF and DMF.
2. The YYF and BLJ tectonic boundaries are crustal-scale faults. The DMF does not exhibit clear crustal-scale offsets near the main fault branch; however, it is also a whole-crustal fault in the northern extension region, indicating structural differences between the north and south of the DMF.
3. East of the TLFZ, we observed a significant low-velocity anomaly and seismic activity in the NCC. This suggests that the eastern side of the fault zone is hotter than the western side, indicating that the destruction of the North China Craton to the east of the fault has been more intense.

Data Availability Statement

The waveforms containing teleseismic data and ambient noise cross-correlations of the portable stations in NCISP10 and NCISP11 are available at (T. Yang, 2024). The Joint inversion of Receiver Function and Surface Wave Dispersion by Hamiltonian Monte Carlo Method software package (T. Yang et al., 2024) was utilized for joint inversion. The hk1.3 software package (Zhu, 2009) was utilized for calculating receiver functions and performing H-κ stacking. The ccp1.0 codes (Zhu, 2009) were employed for CCP stacking of receiver functions. The catalog was downloaded from the IESDC (International Earthquake Science Data Center, 2007).

Acknowledgments

Acknowledgments are extended to the IGGCAS Seismic Array Laboratory and the field crew members who collected the data utilized in this study for their invaluable support. We are grateful to Drs. Weiyu Dong and Lixue Ma for assistance with calculating receiver functions and Rayleigh wave phase velocities. We are grateful to Drs. Nanqiao Du, Shi Yao, Yuchen Wang, Mijian Xu, and Junliu Suwen for the assistance with data processing and joint inversion. We are grateful to Profs. Peng Peng, Xiaohui Zhang, Guang Zhu, Miao Dong, and Chenglong Wu, for their valuable discussions and insights in interpreting our findings. We would like to thank the National Natural Science Foundation of China (42130807, 91955210, 42104102) and the Chinese National Key Research and Development Program (2016YFC0600101) for funding.

References

Aleardi, M., Salusti, A., & Pierini, S. (2020). Transdimensional and Hamiltonian Monte Carlo inversions of Rayleigh-wave dispersion curves: A comparison on synthetic datasets. *Near Surface Geophysics*, *18*(5), 515–543. https://doi.org/10.1002/nsg.12100

Bensen, G., Ritzwoller, M., Barmin, M., Levshin, A. L., Lin, F., Moschetti, M., et al. (2007). Processing seismic ambient noise data to obtain reliable broad-band surface wave dispersion measurements. *Geophysical Journal International*, *169*(3), 1239–1260. https://doi.org/10.1111/j.1365-246X.2007.03374.x

Brocher, T. M. (2005). Empirical relations between elastic wavespeeds and density in the Earth's crust. *Bulletin of the Seismological Society of America*, *95*(6), 2081–2092. https://doi.org/10.1785/0120050077

Cai, J., Liu, F., Liu, P., & Wang, F. (2020). Metamorphic P–T evolution and tectonic implications of pelitic granulites in the Ji'an area, northeastern Jiao–Liao–Ji Belt, North China Craton. *Journal of Asian Earth Sciences*, *191*, 104197. https://doi.org/10.1016/j.jseaes.2019.104197

Chen, Y., Liang, X., Yan, H., Jiang, M., & Ai, Y. (2020). Seismicity of the northern section of the Tanlu fault zone in the Bohai Bay and its implications. *Chinese Journal of Geophysics*, *63*(7), 2566–2578. https://doi.org/10.6038/cjg2020N0159

Christensen, N. (1996). Poisson's ratio and crustal seismology. *Journal of Geophysical Research*, *101*(B2), 3139–3156. https://doi.org/10.1029/95JB03446

Dahlen, F., & Tromp, J. (1999). *Theoretical global seismology*. Princeton university press. https://doi.org/10.1515/9780691216157

Deng, Y., Fan, W., Zhang, Z., & Badal, J. (2013). Geophysical evidence on segmentation of the Tancheng-Lujiang fault and its implications on the lithosphere evolution in East China. *Journal of Asian Earth Sciences*, *78*, 263–276. https://doi.org/10.1016/j.jseaes.2012.11.006

Dong, W., Xu, T., Ai, Y., Fan, E., Li, L., & Hou, J. (2022). The boundary between the North China Craton and the Central Asian Orogenic Belt in NE China: Seismic evidence from receiver function imaging. *Journal of Asian Earth Sciences*, *237*, 105360. https://doi.org/10.1016/j.jseaes.2012.11.006

Du, N., Li, Z., Hao, T., Xia, X., Shi, Y., & Xu, Y. (2021). Joint tomographic inversion of crustal structure beneath the eastern Tibetan Plateau with ambient noise and gravity data. *Geophysical Journal International*, *227*(3), 1961–1979. https://doi.org/10.1093/gji/ggab299

Fan, Q., Liu, R., Wei, H., Sui, J., & Li, N. (1999). The petrology and geochemistry of Jinlongdingzi modern active volcano in Longgang area. *Acta Petrologica Sinica*, *15*(4), 584–589.

Fan, X., & Chen, Q. (2019). Seismic constraints on the magmatic system beneath the Changbaishan volcano: Insight into its origin and regional tectonics. *Journal of Geophysical Research: Solid Earth*, *124*(2), 2003–2024. https://doi.org/10.1029/2018JB016288

Fan, X., Chen, Q., Ai, Y., Chen, L., Jiang, M., Wu, Q., & Guo, Z. (2021). Quaternary sodic and potassic intraplate volcanism in northeast China controlled by the underlying heterogeneous lithospheric structures. *Geology*, *49*(10), 1260–1264. https://doi.org/10.1130/G48932.1

Faure, M., Lin, W., Monie, P., & Bruguier, O. (2004). Palaeoproterozoic arc magmatism and collision in Liaodong Peninsula (north-east China). *Terra Nova*, *16*(2), 75–80. https://doi.org/10.1111/j.1365-3121.2004.00533.x

Fichtner, A., Zunino, A., & Gebraad, L. (2019). Hamiltonian Monte Carlo solution of tomographic inverse problems. *Geophysical Journal International*, *216*(2), 1344–1363. https://doi.org/10.1093/gji/ggy496

Ge, R., Zhang, Q., Wang, L., Xie, G., Xu, S., Chen, J., & Wang, X. (2010). Tectonic evolution of Songliao Basin and the prominent tectonic regime transition in eastern China. *Geological Review*, *56*(2), 180–195.

Gu, C., Zhu, G., Li, Y., Su, N., Xiao, S., Zhang, S., & Liu, C. (2018). Timing of deformation and location of the eastern Liaoyuan Terrane, NE China: Constraints on the final closure time of the Paleo-Asian Ocean. *Gondwana Research*, *60*, 194–212. https://doi.org/10.1016/j.gr.2018.04.012

Gu, C., Zhu, G., Zhai, M., Lin, S., Song, L., & Liu, B. (2016). Features and origin time of Mesozoic strike-slip structures in the Yilan-Yitong Fault Zone. *Science China Earth Sciences*, *59*(12), 2389–2410. https://doi.org/10.1007/s11430-016-5334-4

Gu, C., Zhu, G., Zhang, S., Liu, C., Li, Y., Lin, S., & Wang, W. (2017). Cenozoic evolution of the Yilan–Yitong Graben in NE China: An example of graben formation controlled by pre-existing structures. *Journal of Asian Earth Sciences*, *146*, 168–184. https://doi.org/10.1016/j.jseaes.2017.05.024

Guo, Z., Chen, Y., Ning, J., Feng, Y., Grand, S., Niu, F., et al. (2015). High resolution 3-D crustal structure beneath NE China from joint inversion of ambient noise and receiver functions using NECESSArray data. *Earth and Planetary Science Letters*, *416*, 1–11. https://doi.org/10.1016/j.epsl.2015.01.044

Guo, Z., Chen, Y., Ning, J., Yang, Y., Afonso, J., & Tang, Y. (2016). Seismic evidence of on-going sublithosphere upper mantle convection for intra-plate volcanism in Northeast China. *Earth and Planetary Science Letters*, *433*, 31–43. https://doi.org/10.1016/j.epsl.2015.09.035

Guo, Z., Wang, K., Yang, Y., Tang, Y., John, C., & Hung, S. (2018). The origin and mantle dynamics of quaternary intraplate volcanism in Northeast China from joint inversion of surface wave and body wave. *Journal of Geophysical Research: Solid Earth*, *123*(3), 2410–2425. https://doi.org/10.1002/2017JB014948

Guo, Z., Yang, Y., & Chen, Y. (2016). Crustal radial anisotropy in Northeast China and its implications for the regional tectonic extension. *Geophysical Journal International*, *207*(1), 197–208. https://doi.org/10.1093/gji/ggw261

Hao, Y., Xia, Q., Jia, Z., Zhao, Q., Li, P., Feng, M., & Liu, S. (2016). Regional heterogeneity in the water content of the Cenozoic lithospheric mantle of Eastern China. *Journal of Geophysical Research: Solid Earth*, *121*(2), 517–537. https://doi.org/10.1002/2015JB012105

Huang, S., Dong, S., Zhang, Y., Zhang, F., Huang, D., Wei, S., et al. (2015). The deformation and tectonic evolution of the Huahui basin, northeast China, during the Cretaceous–early Cenozoic. *Journal of Asian Earth Sciences*, *114*, 717–731. https://doi.org/10.1016/j.jseaes.2015.05.013

International Earthquake Science Data Center. (2007). Earthquake catalog data in Northeast China from international earthquake science data center [Dataset]. *Institute of Geophysics, China Earthquake Administration*. https://doi.org/10.11998/IESDC

Julià, J., Ammon, C. J., Herrmann, R. B., & Correig, A. M. (2000). Joint inversion of receiver function and surface wave dispersion observations. *Geophysical Journal International*, *143*(1), 99–112. https://doi.org/10.1046/j.1365-246x.2000.00217.x

Knopoff, L., Mueller, S., & Pilant, W. (1966). Structure of the crust and upper mantle in the Alps from the phase velocity of Rayleigh waves. *Bulletin of the Seismological Society of America*, *56*(5), 1009–1044. https://doi.org/10.1785/BSSA0560051009

Kröner, A., Kovach, V., Belousova, E., Hegner, E., Armstrong, R., Dolgopolova, A., et al. (2014). Reassessment of continental growth during the accretionary history of the Central Asian Orogenic Belt. *Gondwana Research*, *25*(1), 103–125. https://doi.org/10.1016/j.gr.2012.12.023

Landau, L. D., & Lifshitz, E. M. (2013). *Course of theoretical physics*. Elsevier.

Langston, C. A. (1977). Corvallis, Oregon, crustal and upper mantle receiver structure from teleseismic P and S waves. *Bulletin of the Seismological Society of America*, *67*(3), 713–724. https://doi.org/10.1785/BSSA0670030713

Langston, C. A. (1979). Structure under Mount Rainier, Washington, inferred from teleseismic body waves. *Journal of Geophysical Research*, *84*(B9), 4749–4762. https://doi.org/10.1029/JB084iB09p04749

Lei, J., Tian, X., Mishra, O. P., & Huang, Z. (2023). Deep structure and dynamics under East Asia. *Journal of Asian Earth Sciences*, *105921*, 105921. https://doi.org/10.1016/j.jseaes.2023.105921

Lei, J., & Zhao, D. (2005). P-wave tomography and origin of the Changbai intraplate volcano in Northeast Asia. *Tectonophysics*, *397*(3–4), 281–295. https://doi.org/10.1016/j.tecto.2004.12.009

Lei, J., Zhao, D., Xu, X., Du, M., Mi, Q., & Lu, M. (2020). P-wave upper-mantle tomography of the Tanlu fault zone in eastern China. *Physics of the Earth and Planetary Interiors*, *299*, 106402. https://doi.org/10.1016/j.pepi.2019.106402

Levshin, A. L., & Ritzwoller, M. H. (2001). Automated detection, extraction, and measurement of regional surface waves. In *Monitoring the comprehensive nuclear-test-ban treaty: Surface waves* (pp. 1531–1545).

Li, S., Zhao, G., Sun, M., Han, Z., Luo, Y., Hao, D., & Xia, X. (2005). Deformation history of the Paleoproterozoic Liaohe assemblage in the eastern block of the North China Craton. *Journal of Asian Earth Sciences*, *24*(5), 659–674. https://doi.org/10.1016/j.jseaes.2003.11.008

Li, S., Zhao, S., Liu, X., Cao, H., Yu, S., Li, X., et al. (2018). Closure of the Proto-Tethys Ocean and Early Paleozoic amalgamation of microcontinental blocks in East Asia. *Earth-Science Reviews*, *186*, 37–75. https://doi.org/10.1016/j.earscirev.2017.01.011

Li, W., Chen, Y., Tan, P., & Yuan, X. (2020). Geodynamic processes of the continental deep subduction: Constraints from the fine crustal structure beneath the Pamir plateau. *Science China Earth Sciences*, *63*(5), 649–661. https://doi.org/10.1007/s11430-019-9587-3

Ligorría, J. P., & Ammon, C. J. (1999). Iterative deconvolution and receiver-function estimation. *Bulletin of the Seismological Society of America*, *89*(5), 1395–1400. https://doi.org/10.1785/BSSA0890051395

Ling, Y., Zhang, J., Liu, K., Ge, M., Wang, M., & Wang, J. (2017). Geochemistry, geochronology, and tectonic setting of Early Cretaceous volcanic rocks in the northern segment of the Tan–Lu Fault region, northeast China. *Journal of Asian Earth Sciences*, *144*, 303–322. https://doi.org/10.1016/j.jseaes.2016.12.025

Liu, C., Zhu, G., Xie, C., Zhang, S., Li, Y., Su, N., & Xiao, S. (2019). Location and sinistral displacement of the eastern Liaoyuan accretionary belt along the Tan–Lu fault zone, NE China. *Journal of Asian Earth Sciences*, *172*, 409–422. https://doi.org/10.1016/j.jseaes.2018.10.002

Liu, Y., Li, W., Feng, Z., Wen, Q., Neubauer, F., & Liang, C. (2017). A review of the Paleozoic tectonics in the eastern part of Central Asian Orogenic Belt. *Gondwana Research*, *43*, 123–148. https://doi.org/10.1016/j.gr.2016.03.013

Lu, X., Wu, F., Guo, J., Wilde, S. A., Yang, J., Liu, X., & Zhang, X. (2006). Zircon U–Pb geochronological constraints on the Paleoproterozoic crustal evolution of the Eastern block in the North China Craton. *Precambrian Research*, *146*(3–4), 138–164. https://doi.org/10.1016/j.precamres.2006.01.009

Luo, Y., Sun, M., Zhao, G., Li, S., Ayers, J. C., Xia, X., & Zhang, J. (2008). A comparison of U–Pb and Hf isotopic compositions of detrital zircons from the North and South Liaohe Groups: Constraints on the evolution of the Jiao-Liao-Ji Belt, North China Craton. *Precambrian Research*, *163*(3–4), 279–306. https://doi.org/10.1016/j.precamres.2008.01.002

Luo, Y., Yang, Y., Xu, Y., Xu, H., Zhao, K., & Wang, K. (2015). On the limitations of interstation distances in ambient noise tomography. *Geophysical Journal International*, *201*(2), 652–661. https://doi.org/10.1093/gji/ggv043

Ma, C., Lei, J., & Xu, X. (2020). Three-dimensional shear-wave velocity structure under the Weifang segment of the Tanlu fault zone in eastern China inferred from ambient noise tomography with a short-period dense seismic array. *Physics of the Earth and Planetary Interiors*, *309*, 106590. https://doi.org/10.1016/j.pepi.2020.106590

Ma, L., Xu, T., Ai, Y., Yang, J., Yang, Y., Fan, E., et al. (2022). Hot lithosphere beneath the northeastern North China Craton detected by ambient noise tomography. *Tectonophysics*, *839*, 229551. https://doi.org/10.1016/j.tecto.2022.229551

MacKay, D. J. (2003). *Information theory, inference and learning algorithms*. Cambridge university press. Retrieved from https://www.cambridge.org/0521642981

Meng, F., Ai, Y., Xu, T., Chen, L., Wang, X., & Li, L. (2021). Lithospheric structure beneath the boundary region of North China Craton and Xing Meng Orogenic Belt from S-receiver function analysis. *Tectonophysics*, *818*, 229067. https://doi.org/10.1016/j.tecto.2021.229067

Menzies, M., Xu, Y., Zhang, H., & Fan, W. (2007). Integration of geology, geophysics and geochemistry: A key to understanding the North China Craton. *Lithos*, *96*(1–2), 1–21. https://doi.org/10.1016/j.lithos.2006.09.008

Montagner, J. P., & Nataf, H. C. (1986). A simple method for inverting the azimuthal anisotropy of surface waves. *Journal of Geophysical Research*, *91*(B1), 511–520. https://doi.org/10.1029/JB091iB01p00511

Nakata, N., Gualtieri, L., & Fichtner, A. (2019). *Seismic ambient noise*. Cambridge University Press. Retrieved from https://www.cambridge.org/9781108417082

Peng, C., Xue, L., Zhu, M., Chai, Y., & Liu, W. (2016). The location and evolution of the tectonic boundary between the Paleoproterozoic Jiao-Liao-Ji Belt and the Longgang Block, northeast China. *Precambrian Research*, *272*, 18–38. https://doi.org/10.1016/j.precamres.2015.10.016

Phinney, R. A. (1964). Structure of the Earth's crust from spectral behavior of long-period body waves. *Journal of Geophysical Research*, *69*(14), 2997–3017. https://doi.org/10.1029/JZ069i014p02997s

Plank, T., & Forsyth, D. W. (2016). Thermal structure and melting conditions in the mantle beneath the Basin and Range province from seismology and petrology. *Geochemistry, Geophysics, Geosystems*, *17*(4), 1312–1338. https://doi.org/10.1002/2015GC006205

Sambridge, M., Gallagher, K., Jackson, A., & Rickwood, P. (2006). Trans-dimensional inverse problems, model comparison and the evidence. *Geophysical Journal International*, *167*(2), 528–542. https://doi.org/10.1111/j.1365-246X.2006.03155.x

Santosh, M., Sajeev, K., Li, J., Liu, S., & Itaya, T. (2009). Counterclockwise exhumation of a hot orogen: The Paleoproterozoic ultrahigh-temperature granulites in the North China Craton. *Lithos*, *110*(1–4), 140–152. https://doi.org/10.1016/j.lithos.2008.12.010

Schettino, A., & Scotese, C. R. (2005). Apparent polar wander paths for the major continents (200 Ma to the present day): A palaeomagnetic reference frame for global plate tectonic reconstructions. *Geophysical Journal International*, *163*(2), 727–759. https://doi.org/10.1111/j.1365-246X.2005.02638.x

Schwartz, G. (1978). Estimating the dimension of a model. *Annals of Statistics*, *6*(2), 461–464. https://doi.org/10.1214/aos/1176344136

Shan, B., Zhou, W., & Xiao, Y. (2021). Lithospheric thermal and compositional structure of South China jointly inverted from multiple geophysical observations. *Science China Earth Sciences*, *64*(1), 148–160. https://doi.org/10.1007/s11430-019-9661-4

Shapiro, N. M., Campillo, M., Stehly, L., & Ritzwoller, M. H. (2005). High-resolution surface-wave tomography from ambient seismic noise. *Science*, *307*(5715), 1615–1618. https://doi.org/10.1126/science.1108339

Shen, W., Ritzwoller, M. H., Kang, D., Kim, Y., Lin, F., Ning, J., et al. (2016). A seismic reference model for the crust and uppermost mantle beneath China from surface wave dispersion. *Geophysical Journal International*, *206*(2), 954–979. https://doi.org/10.1093/gji/ggw175

Shen, W., Ritzwoller, M. H., Schulte-Pelkum, V., & Lin, F. (2013). Joint inversion of surface wave dispersion and receiver functions: A Bayesian Monte-Carlo approach. *Geophysical Journal International*, *192*(2), 807–836. https://doi.org/10.1093/gji/ggs050

Song, X., & Lei, J. (2023). Direct surface-wave tomography under Northeast China: New insights into 3-D crustal S-wave velocity structure and dynamics of intraplate volcanism. *Physics of the Earth and Planetary Interiors*, *334*, 106959. https://doi.org/10.1016/j.pepi.2022.106959

Suwen, J., Chen, Q. F., & Du, N. (2023). Joint inversion of receiver function and surface wave dispersion by Hamiltonian Monte Carlo sampling. *Seismological Research Letters*, *94*(1), 369–384. https://doi.org/10.1785/0220220044

Tang, D., Chen, H., Sun, J., Zhang, H., & Chen, L. (2010). Cenozoic tectonic evolution of the Yitong part of the Tan-lu fault zone and its control on Yitong basin. *Geotectonica et Metallogenia*, *34*(3), 340–348.

Tang, L., Santosh, M., Tsunogae, T., & Maruoka, T. (2016). Paleoproterozoic meta-carbonates from the central segment of the Trans-North China Orogen: Zircon U–Pb geochronology, geochemistry, and carbon and oxygen isotopes. *Precambrian Research*, *284*, 14–29. https://doi.org/10.1016/j.precamres.2016.08.001

Tang, Z., Julià, J., Mai, P. M., Mooney, W. D., & Wu, Y. (2022). Shear-wave velocity structure beneath Northeast China from joint inversion of receiver functions and Rayleigh wave phase velocities: Implications for intraplate volcanism. *Journal of Geophysical Research: Solid Earth*, *127*(5), e2022JB023956. https://doi.org/10.1029/2022JB023956

Thurber, C., Roecker, S., Ellsworth, W., Chen, Y., Lutter, W., & Sessions, R. (1997). Two-dimensional seismic image of the San Andreas Fault in the Northern Gabilan Range, central California: Evidence for fluids in the fault zone. *Geophysical Research Letters*, *24*(13), 1591–1594. https://doi.org/10.1029/97GL01435

Tian, F., Lei, J., & Xu, X. (2020). Teleseismic P-wave crustal tomography of the Weifang segment on the Tanlu fault zone: A case study based on short-period dense seismic array experiment. *Physics of the Earth and Planetary Interiors*, *306*, 106521. https://doi.org/10.1016/j.pepi.2020.106521

Uyeda, S., & Kanamori, H. (1979). Back-arc opening and the mode of subduction. *Journal of Geophysical Research*, *84*(B3), 1049–1061. https://doi.org/10.1029/JB084iB03p01049

Vinnik, L. P. (1977). Detection of waves converted from P to SV in the mantle. *Physics of the Earth and Planetary Interiors*, *15*(1), 39–45. https://doi.org/10.1016/0031-9201(77)90008-5

Wang, F., Duan, Y., Yang, Z., Zhang, C., Zhao, J., Zhang, J., et al. (2008). Velocity structure and active fault of Yanyuan-Mabian seismic zone: The result of high-resolution seismic refraction experiment. *Science in China, Series A D*, *51*(9), 1284–1296. https://doi.org/10.1007/s11430-008-0098-0

Wang, Y., Forsyth, D. W., & Savage, B. (2009). Convective upwelling in the mantle beneath the Gulf of California. *Nature*, *462*(7272), 499–501. https://doi.org/10.1038/nature08552

Wang, Y., & Li, H. (2008). Initial formation and Mesozoic tectonic exhumation of an intracontinental tectonic belt of the northern part of the Taihang Mountain belt, eastern Asia. *The Journal of Geology*, *116*(2), 155–172. https://doi.org/10.1086/529153

Wang, Z., Xu, W., Pei, F., Wang, Z., & Li, Y. (2015). Geochronology and provenance of detrital zircons from late Palaeozoic strata of central Jilin Province, Northeast China: Implications for the tectonic evolution of the eastern Central Asian Orogenic Belt. *International Geology Review*, *57*(2), 211–228. https://doi.org/10.1080/00206814.2014.1002118

Wilde, S. A. (2015). Final amalgamation of the Central Asian Orogenic Belt in NE China: Paleo-Asian Ocean closure versus Paleo-Pacific plate subduction—A review of the evidence. *Tectonophysics*, *662*, 345–362. https://doi.org/10.1016/j.tecto.2015.05.006

Windley, B. F., Alexeiev, D., Xiao, W., Kröner, A., & Badarch, G. (2007). Tectonic models for accretion of the Central Asian Orogenic Belt. *Journal of the Geological Society*, *164*(1), 31–47. https://doi.org/10.1144/0016-76492006-022

Wu, F., Lin, J., Wilde, S. A., & Yang, J. (2005). Nature and significance of the Early Cretaceous giant igneous event in eastern China. *Earth and Planetary Science Letters*, *233*(1–2), 103–119. https://doi.org/10.1016/j.epsl.2005.02.019

Wu, F., Sun, D., Ge, W., Zhang, Y., Grant, M., Wilde, S. A., & Jahn, B. (2011). Geochronology of the Phanerozoic granitoids in northeastern China. *Journal of Asian Earth Sciences*, *41*(1), 1–30. https://doi.org/10.1016/j.jseaes.2010.11.014

Wu, F., Walker, R. J., Ren, X., Sun, D., & Zhou, X. (2003). Osmium isotopic constraints on the age of lithospheric mantle beneath northeastern China. *Chemical Geology*, *196*(1–4), 107–129. https://doi.org/10.1016/S0009-2541(02)00409-6

Xiao, W., Windley, B. F., Hao, J., & Zhai, M. (2003). Accretion leading to collision and the Permian Solonker suture, Inner Mongolia, China: Termination of the central Asian orogenic belt. *Tectonics*, *22*(6). https://doi.org/10.1029/2002TC001484

Xiao, W., Windley, B. F., Sun, S., Li, J., Huang, B., Han, C., et al. (2015). A tale of amalgamation of three Permo-Triassic collage systems in Central Asia: Oroclines, sutures, and terminal accretion. *Annual Review of Earth and Planetary Sciences*, *43*(1), 477–507. https://doi.org/10.1146/annurev-earth-060614-105254

Xu, M., Li, Y., Hou, H., Wang, C., Gao, R., Wang, H., et al. (2017). Structural characteristics of the Yilan–Yitong and Dunhua–Mishan faults as northern extensions of the Tancheng–Lujiang Fault Zone: New deep seismic reflection results. *Tectonophysics*, *706*, 35–45. https://doi.org/10.1016/j.tecto.2017.03.018

Xu, M., Middleton, M. F., Xue, L. F., & Wang, D. P. (2000). Structure of the lithosphere and Mesozoic sedimentary basins in western Liaoning, northern Liaoning, and Songliao, Northeast China. *International Geology Review*, *42*(3), 269–278. https://doi.org/10.1080/00206810009465082

Xu, M., Yu, D., Huang, Z., Tong, P., Hao, S., Ruan, Y., & Han, C. (2022). Crustal and uppermost mantle heterogeneities across the Ailaoshan Red River shear zone, SE Tibet: Implications for Cenozoic magmatic activity. *Journal of Geophysical Research: Solid Earth*, *127*(6), e2021JB023656. https://doi.org/10.1029/2021JB023656

Xu, T., Ai, Y., Wu, C., Chen, L., Fan, E., Li, L., & Dong, W. (2023). Subduction-induced asthenospheric flow around the Songliao Basin in NE China revealed by shear wave splitting measurements of dense seismic arrays. *Journal of Geophysical Research: Solid Earth*, *128*(3), e2022JB026075. https://doi.org/10.1029/2022JB026075

Xu, W., Pei, F., Wang, F., Meng, E., Ji, W., Yang, D., & Wang, W. (2013). Spatial–temporal relationships of Mesozoic volcanic rocks in NE China: Constraints on tectonic overprinting and transformations between multiple tectonic regimes. *Journal of Asian Earth Sciences*, *74*, 167–193. https://doi.org/10.1016/j.jseaes.2013.04.003

Yang, Q., Shi, W., Li, X., Wang, T., & Lin, M. (2024). Structural patterns and ages of Permian-Triassic multistage strike-slip faulting in the Chifeng area, southeastern Inner Mongolia, China: Implications for the final closure of the Paleo-Asian Ocean. *Journal of Asian Earth Sciences*, *263*, 106006. https://doi.org/10.1016/j.jseaes.2024.106006

Yang, T. (2024). The teleseismic data and ambient noise cross-correlations of NCISP10 and NCISP11 seismic array in Northeast China. (Version 1.0) [Dataset]. *World Data Center for Geophysics, Beijing*. https://doi.org/10.12197/2024GA005

Yang, T., Du, N., & Suwen, J. (2024). Joint inversion of receiver function and surface wave dispersion by Hamiltonian Monte Carlo method. (Version 1.1) [Software]. *Zenodo*. https://doi.org/10.5281/zenodo.11089926

Yang, Y., Ritzwoller, M. H., Levshin, A. L., & Shapiro, N. M. (2007). Ambient noise Rayleigh wave tomography across Europe. *Geophysical Journal International*, *168*(1), 259–274. https://doi.org/10.1111/j.1365-246X.2006.03203.x

Yao, H., van der Hilst, R. D., & Montagner, J. P. (2010). Heterogeneity and anisotropy of the lithosphere of SE Tibet from surface wave array tomography. *Journal of Geophysical Research*, *115*(B12). https://doi.org/10.1029/2009JB007142

Yu, Y., Song, J., Liu, K. H., & Gao, S. S. (2015). Determining crustal structure beneath seismic stations overlying a low-velocity sedimentary layer using receiver functions. *Journal of Geophysical Research: Solid Earth*, *120*(5), 3208–3218. https://doi.org/10.1002/2014JB011610

Yuan, H. (2015). Secular change in Archaean crust formation recorded in Western Australia. *Nature Geoscience*, *8*(10), 808–813. https://doi.org/10.1038/ngeo2521

Zhang, B., Lei, J., Yuan, X., Zhang, G., He, J., & Xu, Q. (2020). Detailed Moho variations under Northeast China inferred from receiver function analyses and their tectonic implications. *Physics of the Earth and Planetary Interiors*, *300*, 106448. https://doi.org/10.1016/j.pepi.2020.106448

Zhang, F., Chen, H., Yu, X., Dong, C., Yang, S., Pang, Y., & Batt, G. (2011). Early Cretaceous volcanism in the northern Songliao Basin, NE China, and its geodynamic implication. *Gondwana Research*, *19*(1), 163–176. https://doi.org/10.1016/j.gr.2010.03.011

Zhang, M., Guo, Z., Liu, J., Liu, G., Zhang, L., Lei, M., et al. (2018). The intraplate Changbaishan volcanic field (China/North Korea): A review on eruptive history, magma genesis, geodynamic significance, recent dynamics and potential hazards. *Earth-Science Reviews*, *187*, 19–52. https://doi.org/10.1016/j.earscirev.2018.07.011

Zhang, S., Gao, R., Li, H., Hou, H., Wu, H., Li, Q., et al. (2014). Crustal structures revealed from a deep seismic reflection profile across the Solonker suture zone of the Central Asian Orogenic Belt, northern China: An integrated interpretation. *Tectonophysics*, *612*, 26–39. https://doi.org/10.1016/j.tecto.2013.11.035

Zhang, S., Zhao, Y., Ye, H., Liu, J., & Hu, Z. (2014). Origin and evolution of the Bainaimiao arc belt: Implications for crustal growth in the southern Central Asian orogenic belt. *Bulletin*, *126*(9–10), 1275–1300. https://doi.org/10.1130/B31042.1

Zhao, G., Cawood, P. A., Li, S., Wilde, S. A., Sun, M., Zhang, J., et al. (2012). Amalgamation of the North China Craton: Key issues and discussion. *Precambrian Research*, *222*, 55–76. https://doi.org/10.1016/j.precamres.2012.09.016

Zheng, Q., Liu, C., Tian, Y., & Zhu, H. X. (2018). Seismic imaging of the middle and upper crust by double-difference tomography: The Haicheng earthquake (Ms7.3) in Liaoning Province. *Applied Geophysics*, *15*(1), 125–136. https://doi.org/10.1007/s11770-018-0662-0

Zheng, T., Duan, Y., Xu, W., & Ai, Y. (2017). A seismic model for crustal structure in North China Craton. *Earth and Planetary Physics*, *1*(1), 26–34. https://doi.org/10.26464/epp2017004

Zheng, T., Zhao, L., & Chen, L. (2005). A detailed receiver function image of the sedimentary structure in the Bohai Bay Basin. *Physics of the Earth and Planetary Interiors*, *152*(3), 129–143. https://doi.org/10.1016/j.pepi.2005.06.011

Zhu, L. (2009). Receiver function package (deconvolution and H-κ stacking) hk1.3 (Version 1.3) and Common-Conversion-Point (CCP) stacking codes ccp1.0 (Version 1.0) [Software]. *Saint Louis University*. Retrieved from https://www.eas.slu.edu/People/LZhu/home.html

Zhu, L., & Kanamori, H. (2000). Moho depth variation in southern California from teleseismic receiver functions. *Journal of Geophysical Research*, *105*(B2), 2969–2980. https://doi.org/10.1029/1999JB900322

Zhu, R., Chen, L., Wu, F., & Liu, J. (2011). Timing, scale and mechanism of the destruction of the North China Craton. *Science China Earth Sciences*, *54*(6), 789–797. https://doi.org/10.1007/s11430-011-4203-4

Zhu, R., Xu, Y., Zhu, G., Zhang, H., Xia, Q., & Zheng, T. (2012). Destruction of the North China craton. *Science China Earth Sciences*, *55*(10), 1565–1587. https://doi.org/10.1007/s11430-012-4516-y

References From the Supporting Information

Levin, V., & Park, J. (1997). Crustal anisotropy in the Ural Mountains foredeep from teleseismic receiver functions. *Geophysical Research Letters*, *24*(11), 1283–1286. https://doi.org/10.1029/97GL51321

Rondenay, S. (2009). Upper mantle imaging with array recordings of converted and scattered teleseismic waves. *Surveys in Geophysics*, *30*(4–5), 377–405. https://doi.org/10.1007/s10712-009-9071-5

Tong, P., Chen, C. W., Komatitsch, D., Basini, P., & Liu, Q. (2014). High-resolution seismic array imaging based on an SEM-FK hybrid method. *Geophysical Journal International*, *197*(1), 369–395. https://doi.org/10.1093/gji/ggt508

Zhu, L., & Rivera, L. A. (2002). A note on the dynamic and static displacements from a point source in multilayered media. *Geophysical Journal International*, *148*(3), 619–627. https://doi.org/10.1046/j.1365-246X.2002.01610.x